

RUBIES: JWST/NIRSpec Confirmation of an Infrared-luminous, Broad-line Little Red Dot with an Ionized Outflow

BINGJIE WANG (王冰洁),^{1,2,3} ANNA DE GRAAFF,⁴ REBECCA L. DAVIES,^{5,6} JENNY E. GREENE,⁷ JOEL LEJA,^{1,2,3} GABRIEL B. BRAMMER,^{8,9} ANDY D. GOULDING,⁷ TIM B. MILLER,¹⁰ KATHERINE A. SUESS,^{11,*} ANDREA WEIBEL,¹² CHRISTINA C. WILLIAMS,^{13,14} RACHEL BEZANSON,¹⁵ LEINDERT A. BOOGAARD,⁴ NIKKO J. CLERI,^{16,17} MICHAELA HIRSCHMANN,¹⁸ HARLEY KATZ,¹⁹ IVO LABBÉ,²⁰ MICHAEL V. MASEDA,²¹ JORRYT MATTHEE,²² IAN MCCONACHIE,²³ ROHAN P. NAIDU,^{24,*} PASCAL A. OESCH,^{12,8} HANS-WALTER RIX,⁴ DAVID J. SETTON,^{7,†} AND KATHERINE E. WHITAKER^{25,8}

¹Department of Astronomy & Astrophysics, The Pennsylvania State University, University Park, PA 16802, USA

²Institute for Computational & Data Sciences, The Pennsylvania State University, University Park, PA 16802, USA

³Institute for Gravitation and the Cosmos, The Pennsylvania State University, University Park, PA 16802, USA

⁴Max-Planck-Institut für Astronomie, Königstuhl 17, D-69117, Heidelberg, Germany

⁵Centre for Astrophysics and Supercomputing, Swinburne University of Technology, Hawthorn, Victoria 3122, Australia

⁶ARC Centre of Excellence for All Sky Astrophysics in 3 Dimensions (ASTRO 3D), Australia

⁷Department of Astrophysical Sciences, Princeton University, Princeton, NJ 08544, USA

⁸Cosmic Dawn Center (DAWN), Copenhagen, Denmark

⁹Niels Bohr Institute, University of Copenhagen, Jagtvej 128, Copenhagen, Denmark

¹⁰Center for Interdisciplinary Exploration and Research in Astrophysics (CIERA) and Department of Physics & Astronomy, Northwestern University, IL 60201, USA

¹¹Kavli Institute for Particle Astrophysics and Cosmology and Department of Physics, Stanford University, Stanford, CA 94305, USA

¹²Department of Astronomy, University of Geneva, Chemin Pegasi 51, 1290 Versoix, Switzerland

¹³NSF's National Optical-Infrared Astronomy Research Laboratory, Tucson, AZ 85719, USA

¹⁴Steward Observatory, University of Arizona, Tucson, AZ 85721, USA

¹⁵Department of Physics & Astronomy and PITT PACC, University of Pittsburgh, Pittsburgh, PA 15260, USA

¹⁶Department of Physics and Astronomy, Texas A&M University, College Station, TX, 77843-4242 USA

¹⁷George P. and Cynthia Woods Mitchell Institute for Fundamental Physics and Astronomy, Texas A&M University, College Station, TX, 77843-4242 USA

¹⁸Institute of Physics, Lab for galaxy evolution, EPFL, Observatoire de Sauverny, Chemin Pegasi 51, 1290 Versoix, Switzerland

¹⁹Sub-department of Astrophysics, University of Oxford, Oxford OX1 3RH, UK

²⁰Centre for Astrophysics and Supercomputing, Swinburne University of Technology, Melbourne, VIC 3122, Australia

²¹Department of Astronomy, University of Wisconsin-Madison, Madison, WI 53706, USA

²²Institute of Science and Technology Austria (ISTA), Am Campus 1, 3400 Klosterneuburg, Austria

²³Department of Physics and Astronomy, University of California, Riverside, Riverside, CA 92521, USA

²⁴MIT Kavli Institute for Astrophysics and Space Research, Cambridge, MA 02139, USA

²⁵Department of Astronomy, University of Massachusetts, Amherst, MA 01003, USA

ABSTRACT

The JWST discovery of “little red dots” (LRDs) is reshaping our picture of the early Universe, yet the physical mechanisms driving their compact size and UV-optical colors remain elusive. Here we report an unusually bright LRD ($z_{\text{spec}} = 3.1$) observed as part of the RUBIES program. This LRD exhibits broad emission lines ($\text{FWHM} \sim 4000 \text{ km s}^{-1}$), a blue UV continuum, a clear Balmer break and a red continuum sampled out to rest-frame $4 \mu\text{m}$ with MIRI. We develop a new joint galaxy and active galactic nucleus (AGN) model within the **Prospector** Bayesian inference framework and perform spectrophotometric modeling using NIRCам, MIRI, and NIRSpec/Prism observations. Our fiducial model reveals a $M_* \sim 10^9 M_\odot$ galaxy alongside a dust-reddened AGN driving the optical emission. Explaining the rest-frame optical color as a reddened AGN requires $A_V \gtrsim 3$, suggesting that a great majority of the accretion disk energy is re-radiated as dust emission. Yet, despite clear AGN

signatures, we find a surprising lack of hot torus emission, which implies that either the dust emission in this object must be cold, or the red continuum must instead be driven by a massive, evolved stellar population of the host galaxy—seemingly inconsistent with the high EW broad lines ($H\alpha$ rest-frame $EW \sim 800 \text{ \AA}$). The widths and luminosities of $Pa-\beta$, $Pa-\delta$, $Pa-\gamma$, and $H\alpha$ imply a modest black hole mass of $M_{BH} \sim 10^8 M_{\odot}$. Additionally, we identify a narrow blue-shifted $He I \lambda 1.083 \mu m$ absorption feature in NIRSpec/G395M spectra, signaling an ionized outflow with kinetic energy up to $\sim 1\%$ the luminosity of the AGN. The low redshift of RUBIES-BLAGN-1 combined with the depth and richness of the JWST imaging and spectroscopic observations provide a unique opportunity to build a physical model for these so-far mysterious LRDs, which may prove to be a crucial phase in the early formation of massive galaxies and their supermassive black holes.

Keywords: Active galactic nuclei (16) – AGN host galaxies (2017) – Galaxy kinematics (602) – Galaxy formation (595) – Photoionization (2060) – Spectral energy distribution (2129)

1. INTRODUCTION

Observations from the James Webb Space Telescope (JWST) have unveiled an intriguing sample of extremely red sources. As they typically also show a compact morphology these objects have been named “little red dots” (LRDs; [Matthee et al. 2023](#)), and they are characterized by a red continuum in the rest-frame optical, a faint blue component in the rest-frame ultraviolet (UV), and often broad Balmer lines indicative of active galactic nuclei (AGNs). Spectroscopic follow-up of LRDs selected based on NIRCcam colors has confirmed a surprising ubiquity of broad emission lines, strongly suggesting an AGN component in the rest-frame optical ([Greene et al. 2023](#); [Labbé et al. 2023a](#)).

At the same time, interpreting the spectral energy distributions (SEDs) of the LRDs remains difficult. It is still unclear how to model the different spectral components, and which parts of the SED are galaxy or AGN dominated. Common galaxy-only or AGN-only models struggle to simultaneously describe the blue slope in the rest-frame UV, and the very red slope toward the rest-frame optical. Early joint modeling of the two components (e.g., [Yang et al. 2020](#); [Furtak et al. 2023a](#); [Williams et al. 2023](#); [Vidal-García et al. 2024](#)) has yielded ambiguous interpretations, while no consensus has been reached about whether the UV can be described by scattered AGN light (e.g., [Labbé et al. 2023a](#)), scattered galaxy light (e.g., [Killi et al. 2023](#)), or simply unobscured star formation (e.g., [Matthee et al. 2023](#)).

The infrared (IR) colors pose additional puzzles: the red slope seen in LRDs strongly suggests high dust attenuation, which, when re-emitted in the IR, results

in different spectral shapes depending on the AGN or galaxy nature of the source. AGN are typically associated with the presence of hot dust which will have a steeply rising red continuum at $> 2 \mu m$ ([Lacy et al. 2004](#); [Richards et al. 2006](#); [Urrutia et al. 2012](#)), whereas the near-IR stellar bump at rest-frame $1.6 \mu m$ leads to a bluer spectral slope ([Laurent et al. 2000](#); [Sawicki 2002](#)). A stacking analysis of LRD candidates in JADES ([Eisenstein et al. 2023](#)) has shown a distinct lack of hot dust, yet no definitive conclusion is drawn regarding whether the flat MIRI color precludes the dominance of AGN in the rest optical, given the available data ([Williams et al. 2023](#)). Broader samples selected by requiring both a red rest-optical and blue rest-UV continuum without a compactness criterion seem to be consistent with dusty star-formation ([Pérez-González et al. 2024](#)), sparking further debate between the galaxy or AGN origins of LRDs.

So far spectroscopic observations of LRDs have been limited to relatively small samples ([Kocevski et al. 2023](#); [Harikane et al. 2023](#); [Matthee et al. 2023](#); [Greene et al. 2023](#); [Furtak et al. 2023b](#)), with the majority of available data restricted to JWST/NIRCcam grism and/or JWST/Prism spectroscopy ([Greene et al. 2023](#); [Kokorev et al. 2023](#); [Killi et al. 2023](#)). The inferred number densities are quite high, comprising a few percent of the galaxy population at $z > 5$ (e.g., [Matthee et al. 2023](#)) and $\sim 20\%$ of the broad-line AGNs (e.g., [Harikane et al. 2023](#)). One lensed LRD presents a galaxy size limit of $< 30 \text{ pc}$, and a implied black hole to galaxy mass ratio of at least a few percent ([Furtak et al. 2023b](#)). Understanding how these massive black holes grew as early as $z = 8.5$ ([Kokorev et al. 2023](#)) in such compact galaxies remains an intriguing puzzle (e.g., [Pacucci & Loeb 2024](#); [Silk et al. 2024](#)).

The absence of medium to high-resolution spectra to date has meant that emission lines cannot be robustly

* NHFP Hubble Fellow

† Brinson Prize Fellow

decomposed, preventing robust measurements of gas kinematics. Accordingly, it is also difficult to characterize potential outflows, which are an integral part of AGN feedback (Zakamska & Greene 2014; Rupke et al. 2017; Davies et al. 2020; Laha et al. 2021). As a consequence, it is unclear in which phase of supermassive black hole growth LRDs are. Although NIRCам/grism spectroscopy has provided emission line kinematics for a larger sample of LRDs (Matthee et al. 2023), these observations are limited in wavelength coverage, typically yielding one or two emission lines rather than a suite of diagnostics.

In this paper, we present a bright LRD at a spectroscopic redshift of $z_{\text{spec}} = 3.1034 \pm 0.0002$ that is luminous in the IR and has multiple broad emission lines indicative of an AGN. RUBIES-BLAGN-1 is discovered as part of the RUBIES program (JWST-GO-4233; PIs de Graaff & Brammer), for which we obtained high signal-to-noise spectra in both the JWST/NIRSpec low-resolution Prism and the medium-resolution G395M modes, allowing for an in-depth characterization of the physics of this object. Notably, RUBIES-BLAGN-1 is detected in JWST/MIRI F770W and F1800W imaging from PRIMER (JWST-GO-1837; PI Dunlop).

The structure of this paper is as follows. Section 2 provides an overview of the data, including imaging, selection, and spectroscopy. Section 3 details the SED modeling, emission-line decomposition, and photoionization modeling. Section 4 presents the results on the inferred AGN and host galaxy properties, morphology, gas kinematics, and mass outflow rate. We conclude in Section 5 with discussion of the key findings.

Where applicable, we adopt the best-fit cosmological parameters from the WMAP 9 yr results: $H_0 = 69.32 \text{ km s}^{-1} \text{ Mpc}^{-1}$, $\Omega_M = 0.2865$, and $\Omega_\Lambda = 0.7135$ (Hinshaw et al. 2013), and a Chabrier initial mass function (Chabrier 2003). Unless otherwise mentioned, we report the median of the posterior, and 1σ error bars are the 16th and 84th percentiles.

2. DATA

RUBIES is a spectroscopic survey with JWST/NIRSpec that targets $\sim 4000 - 5000$ NIRCам-selected sources across the UDS and EGS fields using the micro-shutter array (MSA). Observations are obtained with both the low-resolution Prism/CLEAR and medium-resolution G395M/F290LP modes, providing an unprecedented view of red sources at $z > 3$. Unique to RUBIES is its highly complete sampling of the extremes in color-magnitude space. RUBIES-BLAGN-1 was selected with highest priority based on its extreme red color ($F150W - F444W > 3.0 \text{ mag}$)—roughly 10

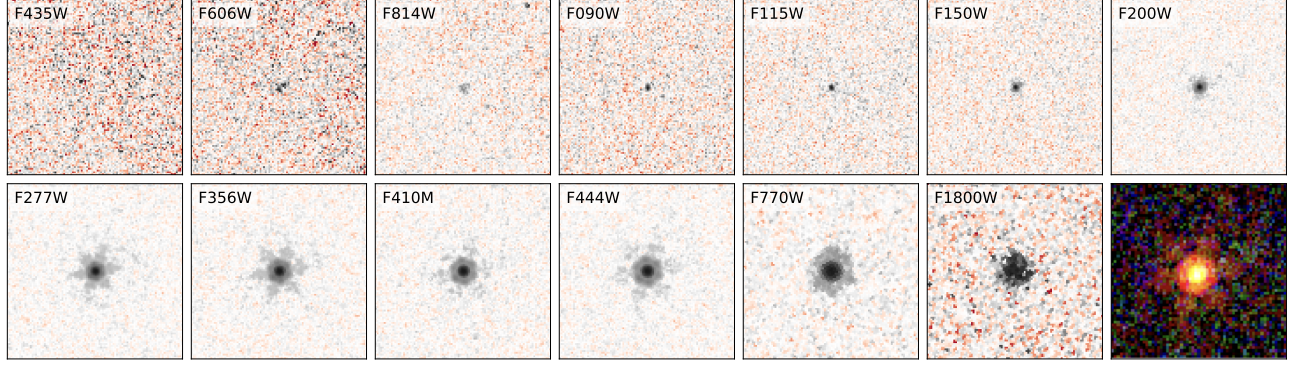
objects in CEERS (Barrufet et al. 2023), and merely 13 objects out of all observed in JADES-GOODS-S (Williams et al. 2023) have such a red color. It is subsequently targeted in two of the three masks observed in January 2024. Full details of the survey design and data reduction will be described in A. de Graaff et al. in prep. This section provides a brief summary of the imaging and spectroscopic data.

2.1. Imaging

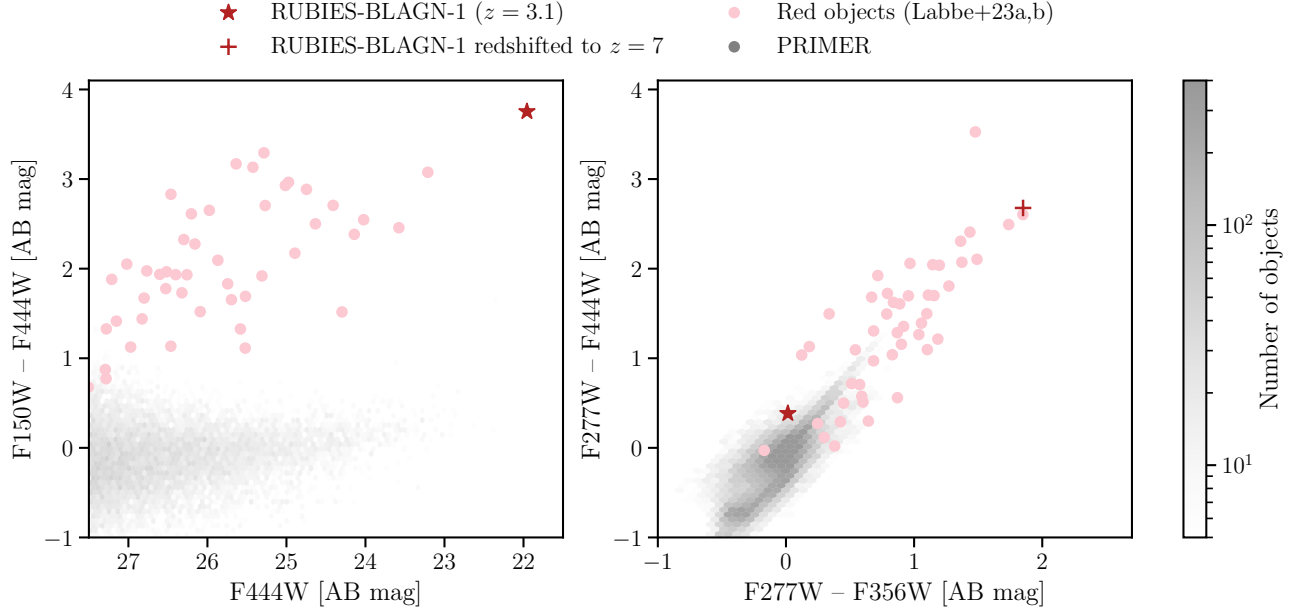
The RUBIES targets in the UDS were selected based on public JWST/NIRCам imaging from the PRIMER survey, which provides NIRCам imaging in 8 bands (F090W, F115W, F150W, F200W, F277W, F356W, F444W and F410M) and MIRI imaging in the F770W and F1800W bands. Archival imaging from the Hubble Space Telescope (HST) is obtained from the CANDELS survey (Grogin et al. 2011; Koekemoer et al. 2011), which adds in 7 more bands in F435W, F606W, F814W, F105W, F125W, F140W, and F160W.

We use the latest version (v7.0) of the publicly available image mosaics from the DAWN JWST Archive (DJA). These images were reduced using *grizli* (Brammer 2023a), as also described in Valentino et al. (2023), and have a pixel scale of $0.04'' \text{ pix}^{-1}$. We run SourceExtractor (Bertin & Arnouts 1996) in dual image mode, using an inverse-variance weighted stack of F277W, F356W and F444W band as the detection image. Next, for each NIRCам band we construct a mosaic that is PSF-matched to the F444W image to measure fluxes in circular apertures with a radius of $0.16''$. We then scale the aperture fluxes to the flux measured through a Kron aperture on a PSF-matched version of the detection image, and to the total flux by dividing by the encircled energy of the Kron aperture on the F444W PSF (A. Weibel et al. in prep).

We use a larger circular aperture of radius $0.35''$ to measure fluxes from the MIRI images. The MIRI images were reduced in August 2023 (v7.0 on the DJA), prior to the release of new photometric calibrations. Following the JWST documentation, we therefore multiply the measured fluxes with a correction factor based on the updated reference file (*jwst_miri_photom_0172*); a factor 0.85 and 1.03 for the F770W and F1800W bands, respectively. Finally, we use the empirical PSF models of Libralato et al. (2023) to scale the MIRI aperture fluxes to total fluxes. This is motivated by our morphological analysis (detailed in Appendix A) which shows that RUBIES-BLAGN-1 is unresolved in the long wavelength images, with a half-light size smaller than a single pixel, $R_e < 0.25 \text{ kpc}$.



(a)



(b)

Figure 1. Photometric observations of RUBIES-BLAGN-1. (a) Cutouts are shown in selected filter bands, including HST/WCS, JWST/NIRCam, and MIRI detections. A color image, composited from NIRCam/F115W, F277W, and F444W, is included as the last panel. Each panel is 5'' in width. (b) RUBIES-BLAGN-1 is bright in F444W (~ 22 AB mag) and exhibits an extreme red color with $F150W - F444W \sim 3.8$ mag. The red objects at higher redshifts are included as pink dots for reference (Labbé et al. 2023a,b). The parent sample, including all sources identified from PRIMER having $F444W < 27.5$ AB mag, is shown in gray. To facilitate a better comparison to the high- z LRDs, the colors of RUBIES-BLAGN-1 interpolated by shifting the observed spectrum to $z = 7$ is plotted as a red plus sign. RUBIES-BLAGN-1 is clearly an outlier in the color space, and possibly can be seen as an analog of the high- z LRDs.

Cutouts for all filters are presented in Figure 1 together with the observed colors of RUBIES-BLAGN-1 and the parent sample, highlighting the extreme color, magnitude, and compactness of the source. For reference, we also put RUBIES-BLAGN-1 on a color-color plot of $F277W - F356W$ vs. $F277W - F444W$ —a criterion used in the literature to select red objects at $z \gtrsim 4$ (Labbé et al. 2023a,b). Clearly RUBIES-BLAGN-1 is an outlier when compared to the parent PRIMER sample.

Shifting the spectrum of RUBIES-BLAGN-1 to $z = 7$ reveals that its colors are similar to those of the high- z LRDs, suggesting it may be taken as a lower-redshift analog.

In addition, we measure upper limits in Spitzer/MIPS 24 μm , Herschel/PACS 100, 160 μm , and Herschel/Spire 250, 350 μm , from the 3D-Herschel project (K. Whitaker et al. in prep). The imaging data is processed following Whitaker et al. (2014), adopting a forced photometry

methodology with the addition of both position and flux priors.

2.2. Spectroscopy

The NIRSpec/MSA low-resolution Prism spectra and the medium-resolution G395M spectra presented in this paper were obtained in two visits between January 16 and 19, 2024. For each visit, RUBIES-BLAGN-1 was observed for 48 min in the Prism/Clear mode and 48 min in the G395M/F290LP mode, using a standard 3-shutter slitlet and 3-point nodding pattern.

The data from the different visits are reduced separately using `msaexp` (Brammer 2023b). We process the uncalibrated NIRSpec exposures (`uncal.fits`) through the Stage 1 steps of the JWST calibration pipeline, inserting an improved mask for “snowball” artifacts between the JumpStep and RampFitStep pipeline procedures using `snowblind`¹. Next, a $1/f$ correction is applied, after which individual slits are identified and the 2D unrectified data are flat fielded. The sky background is removed by taking image differences of the 2D flux-calibrated spectra cut out from the exposures taken at three offset positions with the standard “3-Shutter Nod” offsets. The final 2D spectra are created by rebinning the pixels from each background-subtracted 2D cutout from the original detector frame with curved spectral traces onto a rectified grid with orthogonal wavelength and cross-dispersion axes with weighted nearest-neighbor coaddition. The rectified 2D spectra are then optimally extracted to obtain 1D spectra.

The reduced Prism spectrum from visit 1 and G395M spectra from visits 1 and 2 are shown in Figure 2. Due to the source location on the mask, the Prism spectrum from visit 2 falls largely ($\sim 50\%$ of the trace) in the chip gap between the two NIRSpec detectors. We find that the wavelengths of the emission lines in this spectrum differ significantly from the Prism spectrum of visit 1 and also from the two grating spectra (by $\Delta v \sim 2000 \text{ km s}^{-1}$), and that the flux is a factor 0.75 lower than measured in the other spectra. This likely reflects calibration issues for sources near the edge of the NIRSpec detectors, and in the remainder of the paper we therefore only use the Prism spectrum from visit 1.

To account for the wavelength-dependent slit losses we rescale the Prism spectrum to the NIRCам photometry by fitting a polynomial correction factor within our SED modeling (§ 3.1.1). We then use the best-fit polynomial

for the Prism spectrum to perform a slit loss correction to the G395M data.

3. SPECTRAL MODELING

3.1. Spectral Energy Distribution

3.1.1. Basic Set-up

The available JWST and HST photometric data are jointly fitted with the full NIRSpec/Prism spectrum within the `Prospector` inference framework (Johnson et al. 2021), and the posteriors are sampled using the dynamic nested sampler `dynesty` (Speagle 2020). The joint spectrophotometric fit follows the methodology in Wang et al. (2023a). Here we reiterate the common elements for completeness, before detailing the modifications driven by the peculiar nature of RUBIES-BLAGN-1. Fitting the G395M spectrum simultaneously requires special treatment for the different line spread functions (LSFs) and slit losses, and we leave this for future work.

We convolve the model spectra with the NIRSpec/Prism instrumental resolution curve. We note that the instrumental broadening of NIRSpec for a point source has currently not yet been calibrated empirically. Given the compactness of RUBIES-BLAGN-1, we construct a model LSF using `msafit` (de Graaff et al. 2023) for a point source morphology, which at $4 \mu\text{m}$ is approximately a factor 1.7 narrower than the LSF of a uniformly illuminated slit from the JDox. The resulting resolution from our model is higher, because it accounts for the fact that the spatial extent of the point source in the dispersion direction is narrower than the shutter width. Additionally, to account for the wavelength-dependent slit losses, we fit for a polynomial calibration vector of order 7 after applying a wavelength-independent calibration to scale the normalization of the spectrum to the photometry.

3.1.2. Stellar Populations

To motivate the need for a composite galaxy and AGN model, we start fitting RUBIES-BLAGN-1 with a standard `Prospector` galaxy-only model. Here, no continuum emission from the AGN accretion disk is included, providing a useful baseline against which we can compare the results from our new composite model.

We adopt the MIST stellar isochrones (Choi et al. 2016; Dotter 2016) and MILES stellar spectral library (Sánchez-Blázquez et al. 2006) in FSPS (Conroy & Gunn 2010). The star formation history (SFH) is described by the non-parametric `Prospector- α` model via mass formed in 7 logarithmically-spaced time bins (Leja et al. 2017), with the first bin width decreased to 13.47 Myr to better accommodate the younger age of the universe at $z > 3$ (Wang et al. 2024). A mass function prior and

¹ <https://github.com/mpi-astronomy/snowblind>

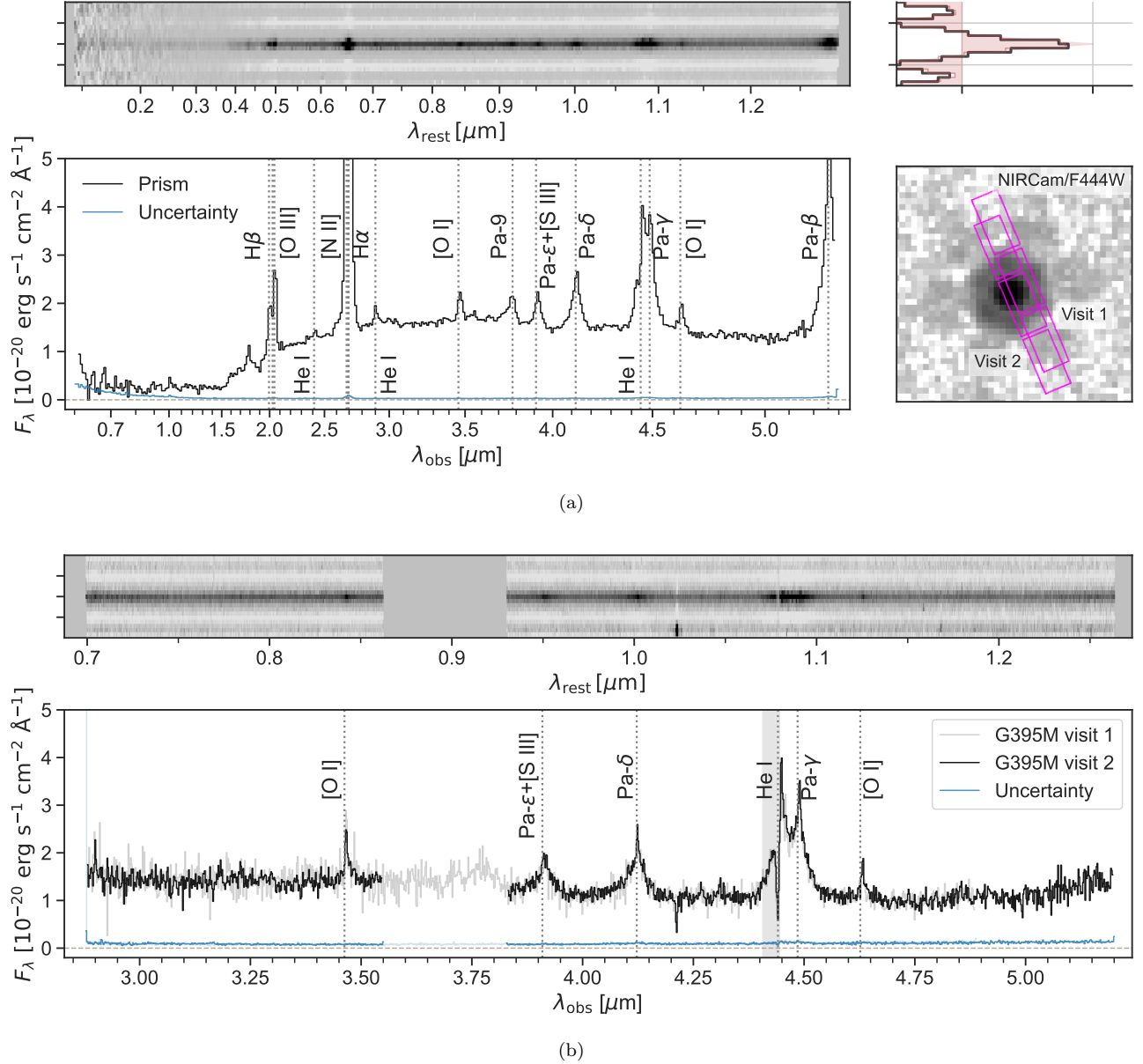


Figure 2. JWST/NIRSpec data of RUBIES-BLAGN-1. (a) The first row displays the 2D Prism spectrum, with the rest-frame wavelength shown along the x -axis; the histogram indicates the extracted region. The left panel in the second row shows the 1D spectrum in F_λ as a function of the observed wavelength. Data and uncertainties are plotted in black and blue, respectively. The beige horizontal line is at $y = 0$ to guide the eye. The cutout in the F444W band is shown to the right, with the slitlets overlaid. (b) Same as the above figure set, but for the G395M visits. Only the 2D spectrum of the second visit is included, which has a higher signal-to-noise ratio.

a dynamic SFH(M, z) prior designed for deep JWST surveys are used as well (Wang et al. 2023b). The normalization and dust optical depth of mid-IR AGNs, as well as dust emission (Draine & Li 2007) are included. We refer the reader to Wang et al. (2024) for a description of the rest of the parameters describing the stellar populations.

3.1.3. AGN Accretion Disk

The observation of unambiguous broad lines in the spectra of RUBIES-BLAGN-1 motivates the modeling of the accretion disk continuum emission. In brief, we approximate the direct UV/optical emission from an AGN accretion disk as piece-wise power laws following Temple et al. (2021). This model is built from SDSS+UKIDSS+WISE AGN and spans the color-luminosity space probed by these surveys. The resulting spectrum of the accretion disk is similar to the SDSS

composite spectrum from [Vanden Berk et al. \(2001\)](#), but mitigates the issue of host galaxy contamination. The normalization of the AGN continuum is a free parameter, parameterized as the ratio of the AGN to stellar flux densities at rest-frame 1500 Å. The power-law slopes are fixed to the best fit values in [Temple et al. \(2021\)](#). Since our wavelength range of interest probes the Rayleigh-Jeans tail of the blackbody emission, we do not expect the slopes to vary significantly across different blackbody temperatures.

As for the dust attenuation, the stellar populations are affected by the diffuse dust, described by a [Calzetti et al. \(2000\)](#) curve with a flexible power-law slope ([Noll et al. 2009](#)). A free parameter is assigned to the fraction of the starlight allowed to live outside the dust screen entirely, suggesting that some of the blue stars have blown holes in the dust or otherwise exist outside it. This is similar to the scenarios invoked to describe the blue rest-UV slopes in otherwise very red sub-millimeter galaxies (e.g., [Hainline et al. 2011](#)). We assume that the light from the accretion disk experiences the same dust attenuation as the stars, but is additionally reddened by a separate dust attenuation curve modeled as a power law with varying normalization and index. In other words, we take the red continuum of RUBIES-BLAGN-1 as indicative of significant dust presence. The range of the power-law attenuation is set such that the flattest slope is Calzetti-like while the steepest slope approximates that of the Small Magellanic Cloud.

Finally, we include a model component that describes hot dust emission from the AGN torus, which typically starts to be observable beyond rest-frame 2 μm . We adopt the torus model implemented in FSPS ([Conroy et al. 2009](#); [Leja et al. 2018](#)), which is based on a simplified CLUMPY model ([Nenkova et al. 2008b](#)) with two free parameters: the normalization and dust optical depth in the mid-IR. In practice, this means that the torus always peaks at the same temperature.

We take the combination of the above AGN accretion disk and torus model and the galaxy model (§ 3.1.2) as the fiducial model of this paper. The relevant parameters are listed in Table 1. However, the unknown nature of LRDs means that other possibilities cannot be ruled out a-priori. We thus additionally fit the data with three alternative models, including fitting with AGN light only, without the new dust component, and fitting the data without the UV continuum. We use these other models to infer the systematic errors in our inferred parameters, and to propose discerning hypotheses for future testing. Details are presented in Appendix B.

3.1.4. AGN Torus

In the above fiducial model, the accretion disk and the torus emissions are independent of each other, meaning that energy balance is not enforced. In other words, the fiducial model does not force the absorbed AGN energy in the rest-UV and optical to be re-emitted into the IR (though energy balance is enforced for the stellar light). This choice is made in light of the concern that the assumption of the attenuated luminosity equaling the emitted luminosity in the IR does not hold in the presence of an angular dependence of dust emission and absorption. Dust emission in a complicated AGN dust torus geometry may have significant inclination dependence, which cannot be modeled with a single unresolved object (e.g., [Nenkova et al. 2008a,b](#)). However, given the existing IR upper limits, we find it valuable to calculate the energy balance. We thus consider two variations on the fiducial model.

First, we ignore the IR limits, and let the total AGN luminosity absorbed by dust in the fiducial model to be re-emitted in the IR. In other words, we scale our simplified CLUMPY torus model spectrum by the luminosity absorbed by the dust. The resulting torus emission is then compared to the IR photometric observations.

Second, we perform the test more broadly on the full CLUMPY model ([Nenkova et al. 2008b](#)). As mentioned earlier, the torus model as implemented in *Prospector* is a simplified version. A wide range of factors can affect the resulting SED of the dust emission; accordingly the CLUMPY model has 6 parameters producing a wide range of observed SED shapes, and other models have a different physical picture entirely with their own associated SED shapes ([Dullemond & van Bemmelen 2005](#); [Hönicig et al. 2006](#)). A detailed characterization of the torus model is out of the scope of this paper. We conduct a simple experiment by randomly drawing CLUMPY models and scaling them to match the total AGN luminosity attenuated by dust. This test allows more freedom in interpreting the IR limits, including in particular extending the range of temperatures in the dust to colder values and allowing variation in the viewing angle.

3.1.5. Emission line Marginalization

In the *Prospector* fit nebular and AGN emission lines are not interpreted using a physical model, but instead described by simple Gaussians using the methodology in [Johnson et al. \(2021\)](#). However, the standard method of using a single Gaussian is insufficient for our case, given the clear broad-line component visible in the observed spectra (Figure 2). We thus implement a two-component Gaussian model for most lines, consisting of

Table 1. AGN and Dust Model Parameters and Priors

Parameter	Description	Prior
$f_{\text{AGN,bbb}}$	ratio between the AGN and the host galaxy’s flux densities at rest-frame 1500 Å, pre-attenuation	log uniform: min = 10^{-5} , max = 500
$f_{\text{AGN,torus}}$	ratio between the AGN luminosity in the mid-IR and the host galaxy’s bolometric luminosity	log uniform: min = 10^{-5} , max = 3
$\tau_{\text{AGN,torus}}$	optical depth of AGN torus dust	log uniform: min = 5, max = 150
$n_{\text{dust},2}$	power law index for a Calzetti et al. (2000) attenuation curve	uniform: min = -1.0 , max = 0.4
$\hat{\tau}_{\text{dust},2}$	optical depth of diffuse dust seen by both the host galaxy and the AGN	uniform: min = 0, max = 4
$n_{\text{dust},4}$	power law index for the AGN-only attenuation curve	uniform: min = -1.8 , max = -0.8
$\hat{\tau}_{\text{dust},4}$	optical depth of dust seen only by the AGN	uniform: min = 0, max = 4
f_{nodust}	fraction of starlight that is not attenuated by the diffuse dust	uniform: min = 0, max = 1

NOTE—The remaining **Prospector** parameters and priors adopted for the stellar population inference are described in [Wang et al. \(2024\)](#).

a narrow and a broad component. We also treat the velocities of the hydrogen lines separately from the metal lines, given the expectation that their line widths can differ from the other lines. This is mostly to ensure sufficient flexibility to accurately describe the lines. A total of four parameters are used to fit the emission lines, i.e., separate velocities for hydrogen lines compared to other lines with a broad and narrow component for each type.

The potential non-Gaussianity of the lines, some of which is visible in Figure 2, is not accounted for. In order to avoid the likelihood being skewed by the residuals from the non-Gaussian line kinematics, we impose a 10% error floor in the spectroscopic data, higher than the 5% error floor usually applied for photometry. We also include a multiplicative noise inflation term as a free parameter, with a prior range from 0.5 to 5, serving as both a pressure valve in the event of significant model mismatch and as an additional check on the quality of the fit.

3.2. Emission-line Decomposition

Separate from the fitting with **Prospector**, we perform kinematic modeling of the brightest broad lines to measure the widths and luminosities of the broad and narrow line components. This separate fit is done to have more fine-tuned understanding of the line kinematics outside of the nested sampling fit. We use the medium-resolution spectra covering 2.9–5.1 μm to measure the properties of the Pa- δ , Pa- γ and He I lines, and fit this complex simultaneously to account for blended lines.

We model each emission line with a broad and narrow Gaussian line profile, and allow for a velocity offset between the two components. We assume uniform priors for the redshift, line fluxes, and velocity dispersions ($\sigma_{\text{broad}} \in [700, 5000] \text{ km s}^{-1}$; $\sigma_{\text{narrow}} \in [0, 700] \text{ km s}^{-1}$). The local continuum is modeled as a 2nd-order polynomial. In addition to this emission model, we find a strong absorption feature at $\approx 4.2 \mu\text{m}$ present in both medium-resolution spectra. This is clearly visible in Figure 2, and a zoom-in is shown in Figure 6. We model this feature as a blue-shifted outflow in the He I $\lambda 10830 \text{ Å}$ line, and assume a Gaussian line profile with uniform priors for the flux, velocity dispersion ($\sigma_{\text{outflow}} \in [0, 1000] \text{ km s}^{-1}$) and velocity offset with respect to the narrow He I component $\Delta v \in [0, 2000] \text{ km s}^{-1}$.

As mentioned in Section 3.1.1, we use a model LSF for a point source morphology ([de Graaff et al. 2023](#)). Although the model LSF has a systematic uncertainty of $\sim 10 - 20\%$, we find in Section 4.5 that the narrow line component is substantially broader than the LSF, and is therefore unaffected. Furthermore, to robustly fit the narrow lines in our data we need to account for the under-sampling of the LSF ($\text{FWHM}_{\text{LSF}} \sim 1 \text{ pix}$) and narrow emission lines. To do so, we construct our model on a wavelength grid that is over-sampled by a factor 5. After convolution with the LSF, the model is integrated and sampled at the original pixel resolution.

We leverage the data from the two independent visits for a better sampling of the LSF. Instead of combining the two spectra, which may introduce further correlated noise, we simultaneously fit to the two spectra. We use

the Markov Chain Monte Carlo (MCMC) ensemble sampling method implemented in **emcee** (Foreman-Mackey et al. 2013) to estimate the posterior distributions of the model parameters.

In addition to our modeling of the medium-resolution data, we also model the low-resolution Prism data, as we find that both the $H\alpha$ and $Pa-\beta$ lines are significantly broader than the Prism LSF. Due to significant issues in the wavelength and flux calibration in the prism spectrum from the 2nd visit, we only use the data from the first visit (i.e., consistent with the **Prospector** modeling). We fit the two lines individually, following a similar approach as for the medium-resolution data, but with some small modifications.

The observed wavelength of $Pa-\beta$ falls on the edge of the spectrum, and the line is therefore partially cut off. With the added complication of the severe under-sampling of the LSF and uncertainty in the LSF, we adjust our model in two ways: (i) we assume that there is no velocity offset between the broad and narrow line, and (ii) we multiply the instrument broadening (σ_{LSF}) by a nuisance parameter f_{LSF} to account explicitly for the uncertainty in the LSF. We assume a truncated Gaussian prior for the latter, with $f_{\text{LSF}} \in [0.8, 1.5]$, a mean of $\mu(f_{\text{LSF}}) = 1.1$ and dispersion $\sigma(f_{\text{LSF}}) = 0.2$ (see Appendix A of de Graaff et al. 2023).

To fit the $H\alpha$ line we additionally include the $[\text{N II}]_{6549,6585}$ doublet in the model. We assume that the $[\text{N II}]$ lines are narrow and equal to the narrow line width of $H\alpha$, and fix the flux ratio of the doublet to 1:2.94. Because the narrow line width is a factor > 4 narrower than the LSF, we cannot constrain the width from the prism data alone. We therefore assume a Gaussian prior for the velocity dispersion of the narrow line based on the estimates from the well-resolved Paschen lines: $\mu(\sigma_{\text{narrow}}) = 250 \text{ km s}^{-1}$ and $\sigma(\sigma_{\text{narrow}}) = 50 \text{ km s}^{-1}$.

3.3. Single-epoch Black Hole Mass

Reverberation mapping can obtain the radius of the broad-line region from the lag between the variability in the AGN continuum and the corresponding variability in the broad permitted lines (e.g., Blandford & McKee 1982). Empirical correlations have since been derived between the radius and line luminosities and widths in the local universe (e.g., Kaspi et al. 2000; Landt et al. 2013). These relationships allow for the black hole mass to be estimated from single-epoch measurements.

Given the wavelength coverage of RUBIES-BLAGN-1, we estimate the black hole mass via three different scaling relations using the Balmer and Paschen series. Comparing these (mostly) independent estimators helps to mitigate the systematic uncertainties introduced by

the application of these methods at higher redshifts and in different physical conditions than where they are calibrated. All line luminosities here are dereddened using the dust attenuation inferred from SED fitting. First, we use the $H\alpha$ scaling relation from Greene & Ho (2005):

$$M_{\text{BH}}/M_{\odot} = 2.0 \cdot 10^6 \cdot \left(\frac{L_{H\alpha}}{10^{42} \text{ erg s}^{-1}} \right)^{0.55} \left(\frac{\text{FWHM}_{H\alpha}}{10^3 \text{ km s}^{-1}} \right)^{2.06}, \quad (1)$$

which has an intrinsic systematic scatter of a factor of ~ 2 .

Second, we adapt the $Pa-\beta$ scaling relation from Kim et al. (2015):

$$M_{\text{BH}}/M_{\odot} = 10^{7.04} \cdot \left(\frac{L_{Pa-\beta}}{10^{42} \text{ erg s}^{-1}} \right)^{0.48} \left(\frac{\text{FWHM}_{Pa-\beta}}{10^3 \text{ km s}^{-1}} \right)^2, \quad (2)$$

which has a lower intrinsic scatter of a factor of ~ 0.2 dex, but is inferred from a smaller reverberation mapping sample (Kim et al. 2010).

Third, we consider the scaling relation between rest-IR Paschen-series lines and the rest-IR continuum (Landt et al. 2013):

$$\log M_{\text{BH}} = 0.88 \cdot \left(2 \log \frac{\text{FWHM}_H}{\text{km s}^{-1}} + 0.5 \log \frac{\nu L_{\nu, 1\mu\text{m}}}{\text{erg s}^{-1}} \right) - 17.39. \quad (3)$$

Although this relation has a high intrinsic scatter of ≈ 1 dex, it allows us to utilize the better determined $Pa-\delta$ and $Pa-\gamma$ lines, and serves as a consistency check.

In addition, we estimate the AGN bolometric luminosity in two ways to facilitate a comparison to the Eddington limit. First, we apply a standard bolometric correction factor of 10 to the dust-corrected luminosity at rest 5100 \AA (e.g., Richards et al. 2006; Shen et al. 2020), and quote this value as our fiducial bolometric luminosity. While imperfect, this model-dependent value represents our best guess for the intrinsic luminosity of the AGN in the context of our preferred AGN model. Second, we base our estimate on the inferred model spectra. We integrate over the observed spectrum with the galaxy contribution subtracted, and then add in the luminosity attenuated by dust. The latter is approximated as the inferred pre-attenuation AGN luminosity, minus the post-attenuation AGN luminosity, based on the dust content from SED fitting. This approximation is likely to be an underestimation, due to the unobserved peak (“big blue bump”; Sanders et al. 1989).

3.4. Photoionization Modeling

We estimate the hydrogen column density associated with the He I absorber by running photoionization models using the C23 version of *Cloudy* (Chatzikos et al. 2023). We adopt the standard AGN radiation field which is a modified version of the Mathews & Ferland (1987) SED with a sub-millimeter break at 10 microns. We calculate a two-dimensional grid of models with hydrogen number density varied in the range $2 < \log(n_{\text{H}})[\text{cm}^{-3}] < 10$ in 0.5 dex steps and ionization parameter varied in the range $-4.5 < \log(U) < 0$ in 0.3 dex steps. The elemental abundances are fixed to solar. The models are run until they reach a hydrogen column density of $\log N_{\text{H}}[\text{cm}^{-2}] = 24$.

For each model, we compute N_{H} and $N_{\text{He}}(2^3S)$ as a function of radius. We use 1D interpolation to find the radius where the predicted $N_{\text{He}}(2^3S)$ most closely matches the measured value, and record the corresponding N_{H} at that radius. Models that do not reach the observed $N_{\text{He}}(2^3S)$ are excluded from further analysis.

4. RESULTS

Several previous studies have attempted to disentangle the AGN or galaxy origin of LRDs. Barro et al. (2023) and Kocevski et al. (2023) suggested that the red continuum can be explained by either a heavily obscured quasar or a dusty starburst galaxy, whereas Labbé et al. (2023a) used ALMA non-detections to infer that the compact red sources are not typical dusty star-forming galaxies. The flat MIRI colors have further led to attempts to model the continuum as a reddened but old stellar population (Williams et al. 2023).

With those ideas in mind, we begin by reporting the size measurements in the long and short wavelengths (§4.1). These may shed light on the AGN or galaxy origins as RUBIES-BLAGN-1 is better resolved owing to its lower redshift. We then proceed to present results from fitting only starlight to the rest UV/optical continuum of RUBIES-BLAGN-1 (§4.2). This model serves as a useful benchmark, against which we evaluate our AGN and galaxy composite model (§4.3). Finally, we explore the family of models that are consistent with the mid-to-far IR data and limits, particularly in the context of dusty torus models that characterize typical AGNs (§4.4). Parameter constraints, including inferred properties of the host galaxy and the AGN are listed in Table 2, and line fluxes and kinematics are listed in Table 3.

4.1. Sizes in the UV and Optical

RUBIES-BLAGN-1 is unresolved in the long wavelength filters, corresponding to the rest-frame optical

emission, with an inferred effective radius of $r_e \leq 0.3$ pixel (≈ 0.1 kpc). However, comparison of the 1D radial profile to the PSF profile as well as 2D Sérsic profile fitting in the F115W filter, suggest that the source is marginally resolved in the rest-frame UV with $r_e = 1.21 \pm 0.21$ pixel (≈ 0.2 kpc). Details on the morphological modeling can be found in Appendix A.

Critically, this analysis is independent of the SED modeling, and already suggests that the UV and rest-frame optical trace different physical components.

4.2. Galaxy-only Best Fit

As seen from Figure 3, the galaxy-only model produces a good fit in the rest-frame UV-optical and an inferred star mass of $\sim 10^{11} M_{\odot}$ with an sSFR of $\sim 10^{-10} \text{ yr}^{-1}$. The rest of the inferred properties are listed in Appendix B, including its mass-weighted age of ~ 0.8 Gyr and A_V of ~ 3 .

It would be unusual but not impossible to have such an old massive galaxy (e.g., the quiescent galaxy at $z_{\text{spec}} = 3.97$, which has $A_V \sim 1.4$ in the center; Setton et al. 2024). It would also be surprising to have such strong broad-line features ($\text{H}\alpha$ rest-frame EW $\sim 800 \text{ \AA}$) and such a massive black hole with very little continuum contribution from the accretion disk, although AGN broad lines may still exist in older galaxies (Carnall et al. 2023). Moreover, the small size of RUBIES-BLAGN-1 (effective radius of ≈ 0.2 kpc in the UV, or < 0.3 kpc conservatively from an upper limit of 1 pixel) implies a very high stellar density (Baggen et al. 2023). This size would also make RUBIES-BLAGN-1 a small galaxy relative to its peers, but not an outlier among known old galaxies at similar mass and redshift (Wright et al. 2023; Ji et al. 2024). However, the inferred narrow line widths of the Pa- γ and Pa- δ lines ($\sim 250 \text{ km s}^{-1}$) and small size imply a dynamical mass $M_{\text{dyn}} \sim 5 R_e \sigma^2 / G \sim 10^{10} M_{\odot}$ (where G is the gravitational constant; see e.g., Cappellari et al. 2006), which would be difficult to reconcile with a stellar mass estimate of $10^{11} M_{\odot}$ even when considering projection effects that may underestimate the true velocity dispersion of the system.

Therefore, we favor the fiducial galaxy and AGN joint fit presented in the following section, but cannot definitively rule out a galaxy-dominated continuum. Follow-up deep medium-resolution data to reveal possible stellar absorption lines, or deeper rest-frame $> 30 \mu\text{m}$ data, will help to discriminate the different scenarios.

4.3. UV/Optical Best Fit

In Figure 4 we show our fiducial galaxy and AGN joint model. An immediate observation is the capability of our fiducial model to generate a very red slope

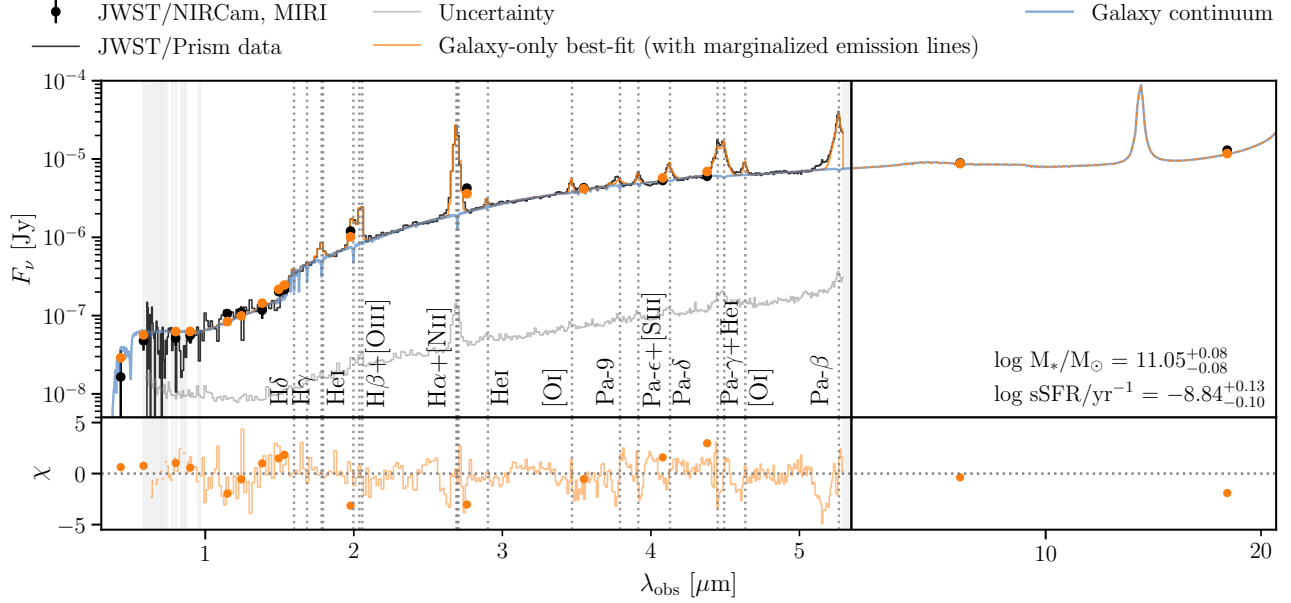


Figure 3. Spectrophotometric modeling with starlight only. The photometric and spectroscopic data are shown in black, whereas the uncertainty in the observed spectrum is shown in gray. The best-fit model spectrum, which includes the marginalized emission lines) is plotted in orange, whereas the unconvolved galaxy model spectrum is over-plotted in blue. The x -axis transits from a linear to a log scale at $5.4 \mu\text{m}$, indicated by the black vertical line, to show the MIRI detections. The spectral regions that are masked due to low S/N, blended, and incomplete lines are shaded in gray. The emission lines included in the marginalization are annotated. χ is included in the bottom.

in the rest optical region and a blue slope in the rest near-UV, providing an effective fit to the observed data. This v-shape in F_λ is difficult to reproduce with a simple AGN-only model (see Appendix B). As depicted in Figure 4, starlight makes up the rest-UV, whereas the light from the reddened AGN accretion disk dominates the spectrum red-ward of rest 4000 \AA .

The model AGN continuum emission is very bright and red due to the large implied dust attenuation and dominates over the wavelength range probed by JWST/MIRI. The torus contributes little to the total light in this fiducial fit even at rest-frame $5 \mu\text{m}$.

The host galaxy has a stellar mass of $\sim 10^9 M_\odot$, and a mass-weighted age of $\sim 0.3 \text{ Gyr}$ ($\sim 15\%$ of the age of the universe). It is metal-poor ($\sim 0.05 Z_\odot$), and slightly below the star-forming main sequence when comparing its sSFR of $\sim 10^{-8.7} M_\odot \text{ yr}^{-1}$ to the value of $\text{sSFR}(M_* \sim 10^9 M_\odot) \sim 10^{-8.3} M_\odot \text{ yr}^{-1}$ as reported in Speagle et al. (2014). The dust attenuation is $A_V \sim 0.5$, with $\sim 10\%$ of the total stars outside the dust screen. The inferred star-formation history resembles that of a post-starburst galaxy, likely driven by the presence of a Balmer break.

The preference for a metal-poor solution is primarily caused by the need to predict the UV excess, since the fiducial model essentially couples the UV light to

the galaxy. A natural question is thus whether the host galaxy properties are heavily influenced by the UV continuum. We address this question by fitting our fiducial model to the rest optical part of the spectrum only in Appendix B. In brief, we find that the inferred stellar mass as well as the inferred star-formation history in this case are similar to those from the fiducial model, suggesting that the UV continuum is not driving the inferred star formation history or mass.

Notably, the above results from SED fitting are consistent with the size measurements: the emission in the rest-frame UV originates from the host galaxy and thus is extended spatially, whereas the rest-frame optical emission is dominated by the AGN that is point-like in nature.

4.4. IR Constraints and an Inability to Model the Mid-IR with a Standard Hot Torus

While our fiducial model does a fine job fitting the rest-frame UV and optical constraints, the MIRI data are surprisingly flat compared to our expectations for a hot dust component from the torus (Bosman et al. 2023). Thus, we consider the alternative modeling assumptions as listed in Section 3.1.4, where we attempt to self-consistently model the reddened AGN disk emission

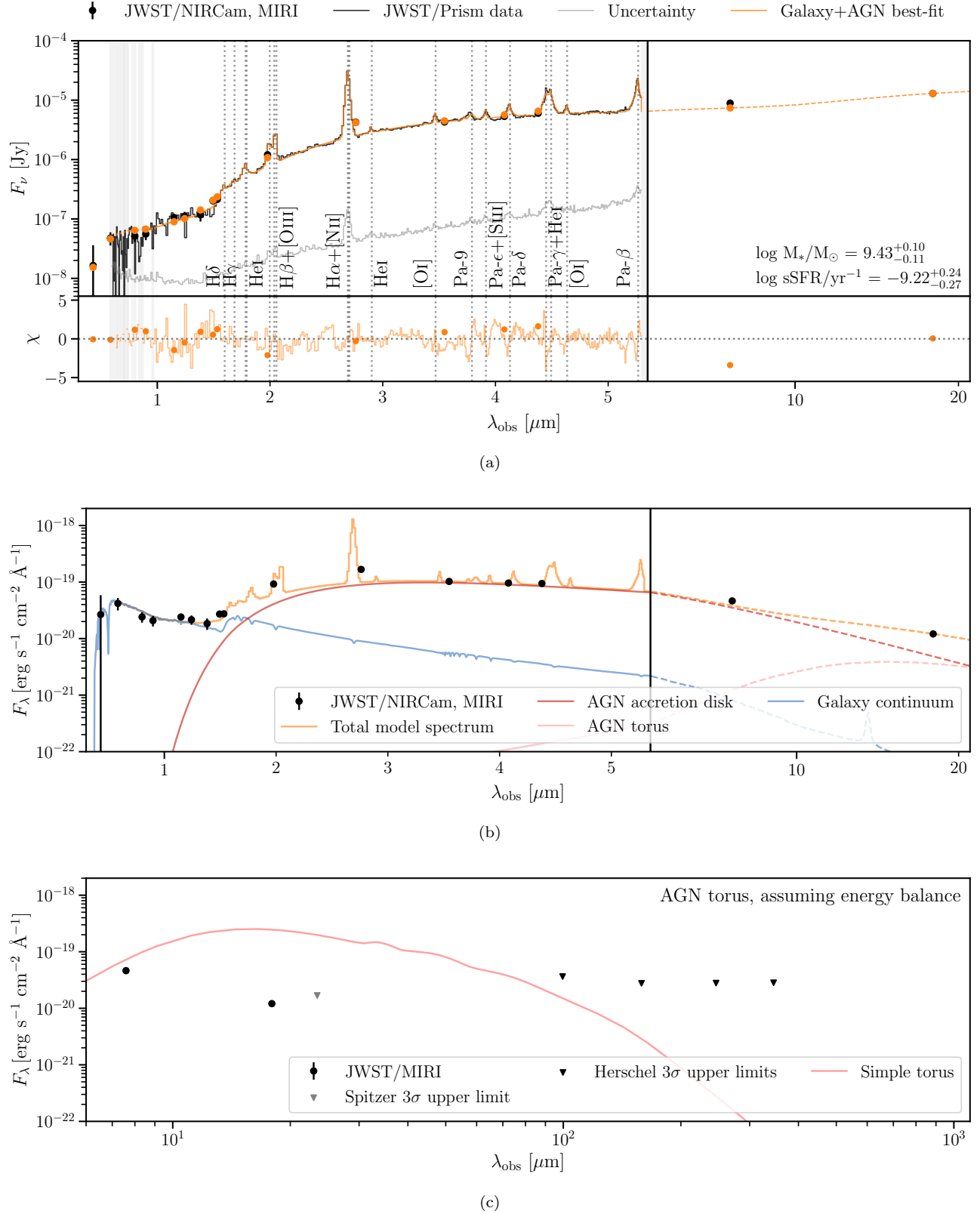
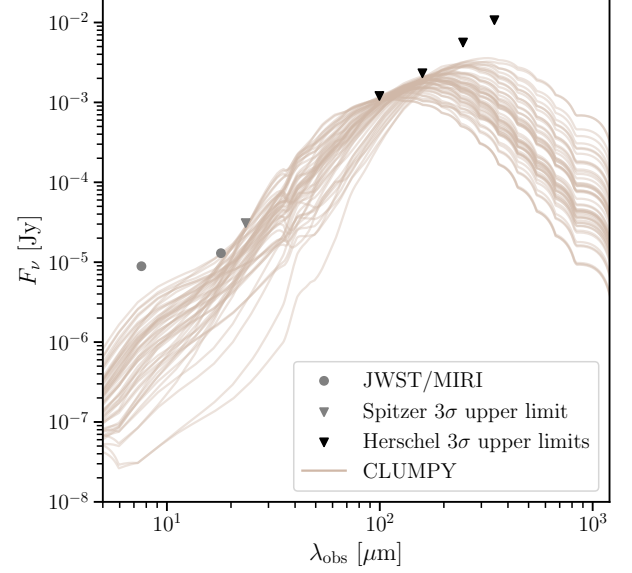


Figure 4. Spectrophotometric modeling with the fiducial AGN and host galaxy composite model. (a) Data and best-fits are shown in the same manner as Figure 3. (b) The various components of the model spectrum are illustrated here. Without assuming energy balance, the model predicts the accretion disk emission dominating the spectrum at $\gtrsim 2 \mu\text{m}$ in the observed frame, with little contribution from the torus. (c) Same model, but letting the attenuated AGN luminosity in the UV/optical to be re-emitted in the IR. The resulting torus emission violates the MIRI detection and the upper limit from Spitzer/MIPS. The black vertical line indicates where the NIRSpc/Prism coverage ends.

Table 2. Inferred Properties of the Host Galaxy and the AGN, and Ancillary Parameters

Basic measurement	
RA [deg]	34.244201
Dec [deg]	-5.245872
z_{spec}	3.1034 ± 0.0002
F150W [AB mag]	25.7 ± 0.05
F277W [AB mag]	22.3 ± 0.05
F356W [AB mag]	22.3 ± 0.05
F444W [AB mag]	21.5 ± 0.01
F1800W [AB mag]	21.1 ± 0.05
Model-inferred property ^a	
$\log M_*/M_\odot$	$9.43^{+0.10}_{-0.11}$
Age [Gyr]	$0.69^{+0.13}_{-0.14}$
SFR [$M_\odot \text{ yr}^{-1}$]	$1.55^{+1.04}_{-0.67}$
$\log \text{sSFR} [\text{yr}^{-1}]$	$-9.22^{+0.24}_{-0.27}$
$\log Z_*/Z_\odot^b$	$-1.27^{+0.67}_{-0.48}$
$\hat{\tau}_{\text{dust},2}$	$0.21^{+0.14}_{-0.09}$
$n_{\text{dust},2}$	$-0.62^{+0.29}_{-0.26}$
f_{nodust}	$0.19^{+0.12}_{-0.11}$
$f_{\text{AGN},7500\text{\AA}}^c$	$11.69^{+3.01}_{-3.87}$
$f_{\text{AGN},\text{torus}}$	$12.11^{+11.34}_{-5.55}$
$\hat{\tau}_{\text{torus}}$	$14.08^{+12.19}_{-5.97}$
$\hat{\tau}_{\text{dust},4}$	$2.79^{+0.12}_{-0.14}$
$n_{\text{dust},4}$	$-1.75^{+0.05}_{-0.03}$
Additional inferred property	
$\log M_{\text{BH}}/M_\odot, \text{H}\alpha$	$8.6 (8.5)^d$
$\log M_{\text{BH}}/M_\odot, \text{Pa}\beta$	$8.4 (8.3)^d$
$\log M_{\text{BH}}/M_\odot, \text{Pa}\delta$	$7.9 (7.8)^d$
$\log M_{\text{BH}}/M_\odot, \text{Pa}\gamma$	$7.9 (7.8)^d$
Bolometric luminosity [L_\odot]	$32 \times 10^{12} (5 \times 10^{12})^e$
Eddington luminosity [L_\odot]	$(2 - 13) \times 10^{12}$

^aPosterior moments from **Prospector**.^bStellar-phase metallicity.^cRatio between the AGN and the host galaxy's flux densities around rest-frame 7500 Å, post-attenuation.^dThe black hole (BH) masses in the first column are estimated assuming the fiducial model, and those in parentheses are based on an alternative dust model (see Appendix B).^eThe bolometric luminosity in the first column are from a standard bolometric correction to the luminosity at rest 5100 Å, and those in parentheses are estimated from the observed spectrum and the inferred dust attenuation.**Figure 5.** Modeling the IR with the CLUMPY torus model (Nenkova et al. 2008b). The JWST photometric data are shown as gray dots, whereas the upper limits from Spitzer/MIPS and Herschel are shown as gray and black triangles, respectively. The curves show random draws that are consistent with the IR upper limits.

and the re-emitted torus dust. The AGN torus spectrum from our fiducial **Prospector** model, re-scaled with the total energy absorbed by dust, is shown in Figure 4 (c). While the model spectrum is marginally consistent with the Herschel upper limits, the MIRI/F1800W and MIPS points are at least a factor of 20 below the predictions from the scaled torus model.

The inability of simple hot AGN torus dust models to explain the observations motivates a more full exploration of the CLUMPY model set (Nenkova et al. 2008b). We draw random models that obey our mid-to-far IR upper limits when scaled by the total energy absorbed by dust, and show 100 examples in Figure 5. This shows that additional freedom in torus clump size, torus shape, and angular dependence of the dust emission and absorption can produce colder AGN dust models which are consistent with the observational constraints. These lower temperatures can be caused by thicker dust shielding which produces a wider and overall colder range of dust temperatures. There is a known population of hot-dust-deficient AGNs which offers further support for this scenario (Hao et al. 2010; Jiang et al. 2010; Mor & Trakhtenbrot 2011; Lyu et al. 2017).

We note that since the AGN bolometric luminosity from L_{5100} may be $\sim 6 - 7$ times higher than that in-

ferred from the continuum model, we perform an additional test where we increase the remitted IR luminosity by a factor of 2. In this case, the full CLUMPY model struggles to produce a torus spectrum that is consistent with the IR limits, just making the challenge to model the torus more accurate.

Three physical scenarios can be invoked to explain the apparent lack of torus emission. First, the dust emission from LRDs may be in a relatively unexplored regime, being colder than any model in the CLUMPY database. Second, a majority of the energy originated from the big blue bump escapes through some combination of anisotropic dust attenuation or hard X-ray photons and so is not absorbed by dust. Third, the UV part of the accretion disk could be suppressed in a super-Eddington flow (e.g., Abramowicz et al. 1988; Kubota & Done 2019). Deeper rest-frame mid/far-IR constraints would help to reveal the nature of the source.

4.5. Gas Kinematics

We show the decomposition into narrow and broad components (§ 3.2) in the Paschen and $H\alpha$ lines in Figure 6, and list the fluxes and velocity dispersions in Table 3. We find that the narrow and broad line widths of the $Pa-\gamma$ and $Pa-\delta$ lines are in good agreement, and that the narrow line flux comprises 14% and 10% of the total line flux, respectively. The narrow and broad line widths of the $Pa-\beta$ emission are broader than the other Paschen lines by approximately 2σ , and with a higher narrow-to-total flux ratio (25%). Although some physical differences may be expected if the different line transitions trace gas in different parts of the broad line region (BLR), the $Pa-\beta$ line is at the very edge of the spectrum which may bias the kinematic fitting. The $H\alpha$ broad line is significantly broader, by a factor ≈ 1.3 , than the Paschen broad lines; the narrow line flux is approximately 30% of the total $H\alpha$ line flux. This may imply that the $H\alpha$ line traces a closer-in region of the BLR compared to the Paschen lines (see e.g., Kim et al. 2010). However, as the narrow $H\alpha$ line and the $[N II]$ lines are unresolved at the resolution of the Prism, the kinematic fit depends on the model assumptions made (at the $\approx 10\%$ level for the broad line width). Follow-up spectroscopy at higher resolution will be crucial to perform more careful modeling of the $H\alpha$ and $[N II]$ emission line complex and robustly constrain the narrow-to-total line flux ratio, and to confirm the difference in the broad line width between the Balmer and Paschen lines.

Interestingly, we find a blue-shifted absorption feature in the wings of the $He I \lambda 1.083 \mu m$ line. The $He I$ absorp-

tion of RUBIES-BLAGN-1 shows up in both G395M spectra, ruling out the possibility of a detector defect. We measure a velocity dispersion of $\sim 240 \text{ km s}^{-1}$, and a velocity offset of $\sim -860 \text{ km s}^{-1}$ with respect to the narrow $He I$ emission. The $He I$ line is associated with the 2^3S metastable state, which is 19.7 eV above the ground state and is primarily populated by recombination from $He II$. Therefore, the absorption line effectively traces ionized gas. This makes it likely that the absorption tracers an outflow from RUBIES-BLAGN-1 rather than intervening gas along the line of sight. In addition, the velocity of the absorber also suggests it is associated with the outflow (e.g., Culliton et al. 2019).

A few other LRDs show absorption features, albeit in the $H\alpha$ line. Whereas Matthee et al. 2023 interpreted this as an outflow feature, Maiolino et al. (2023) proposed a dual AGN explanation. The addition of RUBIES-BLAGN-1 suggests that such outflows may be a common feature among LRDs, although follow-up high-resolution observations of the Balmer lines will be needed to confirm whether the outflow is present in both $He I$ and $H\alpha$. Similar outflows in the $He I$ line have been observed in multiple nearby AGN (e.g. Leighly et al. 2011; Zhang et al. 2017; Pan et al. 2019). However, we note that it is also possible that the $He I$ line profile originates from Wolf-Rayet stars, consistent with the modest velocities (Eenens & Williams 1994; Stevens & Howarth 1999). In this case, the P-Cygni profile is to be interpreted as a stellar wind rather than a galactic wind. Constraints on other possible Wolf-Rayet features will be needed to conclusively rule out the stellar wind scenario.

We estimate the optical depth of the $He I$ absorption by constructing the emission-only spectrum from our kinematic modeling ($f_{\lambda, \text{emission}}$), and integrating over the absorption line (red shaded region; e.g., Savage & Sembach 1991):

$$\tau = \int \ln \left(\frac{f_{\lambda, \text{obs}}}{f_{\lambda, \text{emission}}} \right) d\lambda. \quad (4)$$

The column density, assuming that the source is fully covered by the absorber, is then computed as

$$N_{He}(2^3S) = \frac{m_e c}{\pi e^2 f_0 \lambda_0} \tau, \quad (5)$$

where m_e and e are the electron mass and charge, c is the speed of light, and f_0 and λ_0 are the wavelength and oscillator strength of the line transition. We find $N_{He}(2^3S) = 5.9 \pm 0.3 \times 10^{13} \text{ cm}^{-2}$, where the uncertainty reflects both the uncertainty in the emission-only model and the observed flux density. This measured column density agrees well with measurements of $He I$ absorbers

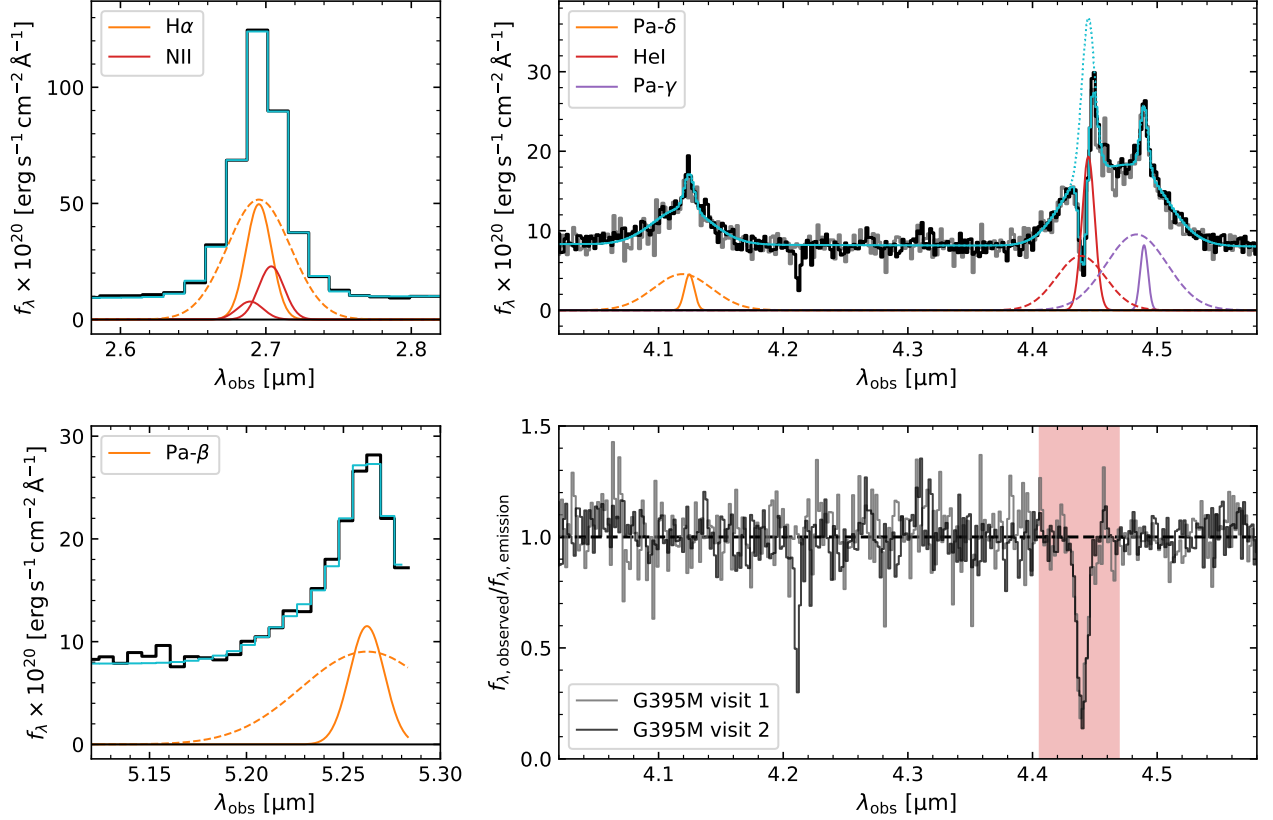


Figure 6. Kinematic emission line decomposition. On the left, we show the emission line fits to the Prism spectrum for the blended H α and [N II] complex (top) and Pa- β line (bottom). Although the narrow line widths are poorly constrained due to the broad LSF (and the partial coverage of Pa- β), the broad lines are well constrained. On the right, we show the results of our fitting for the Pa- δ and blended HeI and Pa- γ lines in the the G395M spectra (top). We find a strong blue-shifted absorption feature in the HeI line in the two independent G395M spectra, which we interpret as an ionized outflow. The bottom right shows the observed spectrum divided by the best-fit model emission spectrum. The red shaded region indicates the area used to integrate the optical depth and compute the column density of the absorbing gas. The absorption feature at 4.2 μm is present in only one of two visits and corresponds to a detector artefact (see Figure 2).

found in nearby AGN (e.g. Zhang et al. 2017; Pan et al. 2019)

4.6. Mass Outflow Rate

We estimate the mass outflow rate from this source using the outputs of the `Cloudy` modeling. The time-averaged mass outflow rate of a spherically symmetric, mass-conserving wind of finite radius is given by

$$\dot{M}_{\text{out}} = 4\pi C_{\Omega} \mu m_p N_H R_{\text{out}} v_{\text{out}}, \quad (6)$$

where μ is the mean atomic mass per proton (1.4), $4\pi C_{\Omega}$ is solid angle subtended by the outflowing material, R_{out} is the outflow size and v_{out} is the outflow velocity (e.g., Rupke et al. 2005). We assume that the absorbing material covers 50% of the solid sphere (i.e. $C_{\Omega} = 0.5$), motivated by the fact that at least 50% of quasars at

$z \sim 2 - 4$ show associated narrow absorption lines (e.g., Misawa et al. 2007).

The hydrogen column density and outflow size cannot be measured directly. However, we can constrain the range of reasonable values through the photoionization modeling. In Section 4.5, we measured a column density of $\log N_{\text{He}}(2^3S)/\text{cm}^{-2} \simeq 13.8$.

The left panel of Figure 7 shows the radius and N_H of the `Cloudy` models when they reach the measured $N_{\text{He}}(2^3S)$. The points are color-coded by the ionization parameter and the symbol sizes indicate the gas density. The observed $N_{\text{He}}(2^3S)$ can be matched by absorbers at a wide range of radii and column densities. Rather than choosing representative values to calculate the mass outflow rate, we compute the mass outflow rate for each grid point individually. The right-hand panel shows the in-

Table 3. Results of the emission line decomposition

Emission	Flux (total)	Flux (narrow)	σ (narrow)	Flux (broad)	σ (broad)	EW (total)
	$10^{-18} \text{ erg s}^{-1} \text{ cm}^{-2}$	$10^{-18} \text{ erg s}^{-1} \text{ cm}^{-2}$	km s^{-1}	$10^{-18} \text{ erg s}^{-1} \text{ cm}^{-2}$	km s^{-1}	rest-frame Å
H α	392^{+15}_{-15}	109^{+22}_{-18}	253^{+50}_{-51}	282^{+18}_{-20}	2228^{+67}_{-63}	832 ± 33
[N II]	67^{+15}_{-15}					143 ± 33
Pa- β	103^{+5}_{-4}	26^{+5}_{-4}	424^{+72}_{-79}	77^{+5}_{-6}	1929^{+149}_{-141}	35 ± 2
Pa- δ	$31.2^{+1.2}_{-1.2}$	$4.4^{+1.0}_{-0.7}$	273^{+62}_{-45}	$26.6^{+1.1}_{-1.1}$	1700^{+114}_{-95}	99 ± 4
Pa- γ	65^{+3}_{-3}	$6.4^{+0.7}_{-0.7}$	196^{+31}_{-26}	59^{+3}_{-3}	1644^{+68}_{-61}	217 ± 10
He I	59^{+5}_{-4}	25^{+4}_{-3}	341^{+28}_{-29}	34^{+3}_{-3}	1327^{+64}_{-64}	192^{+17}_{-14}
Absorption	Outflow flux	$d v_{\text{outflow}}$	σ_{outflow}			EW
	$10^{-18} \text{ erg s}^{-1} \text{ cm}^{-2}$	km s^{-1}	km s^{-1}			rest-frame Å
He I	-25^{+3}_{-4}	-863^{+121}_{-113}	242^{+10}_{-10}			-82^{+10}_{-14}

ferred mass outflow rate as a function of outflow size, as well as the corresponding kinetic luminosity of the outflow, given by $1/2 \dot{M}_{\text{out}} v_{\text{out}}^2$.

There is a strong positive correlation between the radius and the mass outflow rate. The lowest density models reach radii of $10 - 100 \text{ pc}$ with corresponding mass outflow rates of $1 - 200 \text{ M}_{\odot} \text{ yr}^{-1}$. On the other hand, the highest density models imply radii of $< 0.1 \text{ pc}$, which would place the absorber within the AGN broad line region, with corresponding mass outflow rates $< 0.01 \text{ M}_{\odot} \text{ yr}^{-1}$. To constrain this better would require another estimate of the absorber size, more absorption lines, or both.

4.7. Black Hole Mass

The various scaling relations consistently result in black hole masses in the range $\sim 10^{7.9} - 10^{8.6} \text{ M}_{\odot}$. This black hole mass is lower than typical UV-selected quasars at $z \sim 3$ (e.g., Shen & Kelly 2012), but, as it is roughly $8 - 40\%$ of the stellar mass, similar to the unexpected large black hole to stellar mass ratios found at higher redshifts (Goulding et al. 2023; Maiolino et al. 2023).

If we adopt the narrow line widths as $\sigma_{\text{gas}} = 200 - 270 \text{ km/s}$, then we find an expected range of $M_{\text{BH}} = 4 \times 10^7 - 2 \times 10^8 \text{ M}_{\odot}$. These values are consistent with our broad-line scalings, suggesting that while the stellar mass may be catching up, the black hole may still scale with the stellar velocity dispersion (Chisholm et al. 2003; Maiolino et al. 2023).

Given the range of black hole masses, we obtain an Eddington luminosity of $\sim 2 - 13 \times 10^{12} \text{ L}_{\odot}$, implying the black hole radiates at $\sim 40\%$ of the Eddington limit to potentially super-Eddington.

However, we caution that systematic uncertainties, including the intrinsic scatter in the scaling relations and different dust models, which are not accounted for, likely dominate the error budget at $\gtrsim 1$ dex level for the above estimations.

4.8. X-ray Non-detection

RUBIES-BLAGN-1 was observed by the Chandra X-ray Observatory in Cycle 17, as presented by Kocevski et al. (2018). We adopt the exposure maps, event rates, and PSF models from those authors. At the position of RUBIES-BLAGN-1, the effective exposure time is $\approx 170 \text{ ks}$ using the Advanced CCD Imaging Spectrometer-I. Assuming a standard power-law slope of $\Gamma = 1.9$ at $z = 3$ (Wang et al. 2021) and foreground galactic absorption $N_{\text{H}} = 2.01 \times 10^{20} \text{ cm}^{-2}$, we directly measure the restframe 2-10 keV counts at the position of the source. The resulting 3σ upper limit $< 3 \times 10^{43} \text{ erg s}^{-1}$, making the source nearly 100 times fainter than we would naively expect from the dereddened L_{5100} luminosity of $\sim 10^{46} \text{ erg s}^{-1}$. This surprising result is discussed further in Section 5.1.

5. DISCUSSION AND CONCLUSIONS

In this paper, we present spectroscopic observations of a bright IR-luminous broad-line LRD using NIR-Spec/Prism and G395M onboard JWST. We perform spectrophotometric modeling to infer the properties of the host galaxy and the AGN, and decompose the emission and absorption complexes to constrain the gas kinematics and measure the black hole mass. Additionally, we take a first look at the mass outflow rate as implied from the He I $\lambda 1.083 \mu\text{m}$ absorption. Below we discuss the key findings in this work.

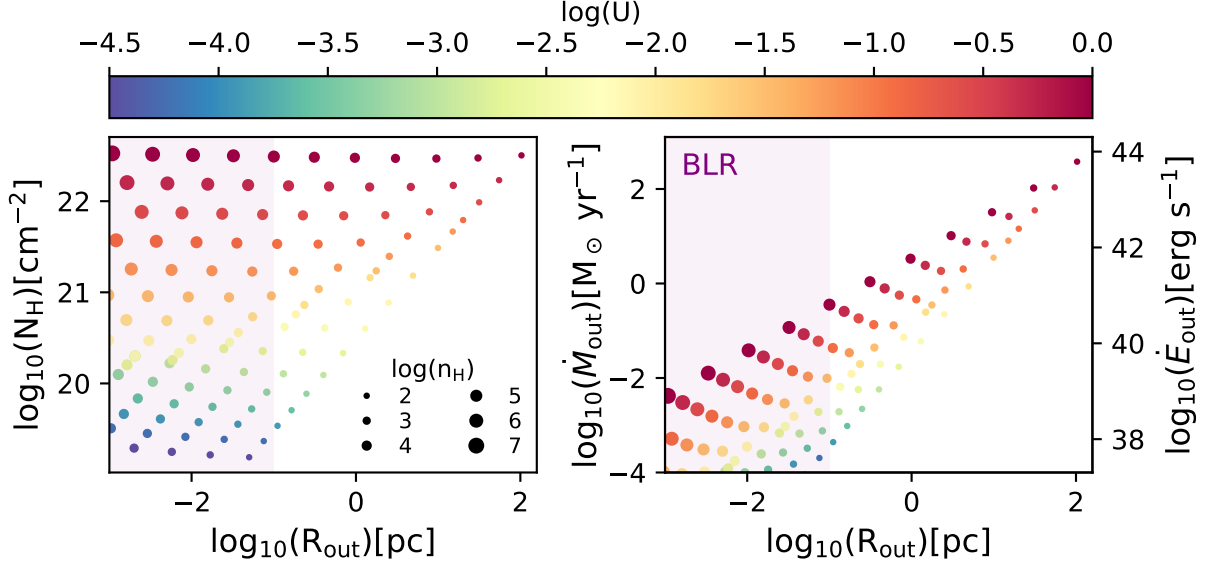


Figure 7. Photoionization modeling with *Cloudy*. (Left) Inferred possible hydrogen column density of the He I absorber is plotted as a function of size. Each point represents a single model, where the color and size indicate the density and ionization parameter of that model, respectively. The purple shaded region covers sizes < 0.1 pc which would approximately represent an origin within the AGN broad line region. (Right) Inferred mass outflow rates are shown in the same manner. The possible mass outflow rates span 6 orders of magnitude, primarily due to the unknown gas density.

5.1. A Spectroscopically Confirmed Broad-line AGN with a Deficit of Hot Dust

RUBIES-BLAGN-1 is an unusually red and bright object compared to the parent RUBIES sample. In this paper, we argue that the bright and red rest-frame optical continuum is likely dominated by AGN light. The presence of an AGN is supported by the broad and symmetric Balmer and Paschen emission lines, strongly suggesting that we are seeing the AGN disk and broad-line region directly (i.e., an unobscured, but highly reddened AGN). In combination with the lack of broadened forbidden lines, the data disfavor an outflow interpretation.

We have developed a novel method to model the host galaxy and AGN within the *Prospector* Bayesian inference framework (Johnson et al. 2021). Our preferred model is a composite AGN and host model, in which the UV and the Balmer break are explained by galaxy light, and the AGN continuum from the outer accretion disk dominates in the optical and mid-IR. These results are further corroborated by our morphological analysis of RUBIES-BLAGN-1, in which we find the source to be marginally resolved in the rest-frame UV, but unresolved at rest-frame optical wavelengths (Appendix A).

Explaining the rest-frame optical continuum light with pure galaxy continuum is possible, but yields a very high mass of $\sim 10^{11} M_{\odot}$. While unresolved in the rest-frame optical, its measured half light radius (< 0.27 kpc

at F277W) would yield an extreme stellar surface density $> 10^{12.4} M_{\odot} \text{ kpc}^{-2}$; even a conservative upper limit of one pixel on its size would yield a very high stellar density $> 10^{11.2} M_{\odot} \text{ kpc}^{-2}$ (in some tension with theoretical density limits from stellar feedback; Hopkins et al. 2010; Grudić et al. 2019) and is inconsistent with the dynamical mass inferred from the narrow Pa- γ and Pa- δ emission lines. Further, a galaxy interpretation also would lead to a very high H α rest-frame EW of $\sim 800 \text{ \AA}$, which is inconsistent with the inferred older stellar populations and also has not been seen in known AGNs (Vanden Berk et al. 2001; Stern & Laor 2012). Likewise, fitting a pure AGN model fails to reproduce the spectral shape around the Balmer break region (Appendix B).

It is worth emphasizing, however, that we cannot rule out a small fraction of the red light coming from a massive galaxy with an older dusty stellar population. This additional stellar component would contribute a lot more mass, potentially amounting to a stellar mass at the order of $10^{10} M_{\odot}$, without violating the main conclusions of a prominent AGN.

The flat (in F_{ν}) spectral shape in the mid-IR also presents a significant challenge to our composite AGN and host galaxy picture since a near-ubiquitous component of AGN at all redshifts is a hot dusty torus that begins to dominate AGN emission longward of $2 \mu\text{m}$.

That component is not observed in this source. In fact, a much larger sample of sources detected in the JADES fields tells the same basic story; while the rest-frame optical appears to require significant obscuration, there is no evidence of emission from the torus itself out to $2 - 5 \mu\text{m}$ in the rest frame (Williams et al. 2023; Pérez-González et al. 2024). In the majority of cases, with the exception of one object from Matthee et al. (2023), this larger sample do not have measurements of broad $H\alpha$, and so RUBIES-BLAGN-1 provides a special case where we can strongly argue for an AGN component despite the lack of hot dust, perhaps refuting the assumption made in Pérez-González et al. (2024) that these sources are best explained by dusty star formation in the majority of cases. However, RUBIES-BLAGN-1 provides clear confirmation that it is possible to both have an unambiguous broad-line AGN dominate the red continuum in the rest frame optical and simultaneously lack the rising hot dust continuum in the mid-IR.

There is another other major puzzle in the SEDs of the LRDs, which is their apparent lack of X-ray emission. Roughly speaking, RUBIES-BLAGN-1 is at least 100 times fainter in the X-ray than we would naively expect from the dereddened L_{5100} . Put together, the dusty optical continuum, lack of hot dust, and lack of X-ray emission mean that while we can fit the observed UV-optical SED, we do not yet have a full understanding of the underlying physical picture. Thus, measurements of the extinction, intrinsic AGN luminosity, and black hole mass should all be viewed as contingent until a more complete picture can be built.

Even considering a wider redshift range, there are limited number of known analog AGNs with this particular set of spectral characteristics. A handful of cases with a deficiency of hot dust emission are known among high-redshift QSOs (Jiang et al. 2010). These are thought to have evolved relatively dust-poor due to their early formation, although similar hot dust deficient AGN also exist at low- z (Hao et al. 2011; Lyu et al. 2017; Brown et al. 2019; Son et al. 2023). No consensus yet exists about the physical origin of the hot dust deficiency, although a potential explanation could be a difference in torus structure (see discussion in Lyu & Rieke 2022). However, known dust-deficient AGNs are also typically blue in the rest-frame optical reflecting low dust obscuration, in stark contrast to the extreme red rest-optical colors of our confirmed RUBIES-BLAGN-1 and LRDs in the literature. Meanwhile, analogous low-luminosity AGN with similarly v-shaped SEDs in the rest-optical/UV (e.g., blue dust obscured galaxies; Noboriguchi et al. 2023) tend to get hot quickly, and are heavily obscured at rest-frame $< 6 \mu\text{m}$, leading to steeply rising SEDs

into the mid-IR. While it could be possible to reconcile these inconsistent SED properties for specific host geometries that strongly attenuate the rest-optical without an obscuring dust torus (e.g., through polar dust instead; Asmus et al. 2016; Stalevski et al. 2019), the fact that statistical samples of LRDs in the literature also exhibit flat mid-IR SEDs (Williams et al. 2023) argues against orientation or geometrical effects giving rise to such unusual SEDs. Thus, to our knowledge, no known class of AGN across redshifts exhibit similar properties to RUBIES-BLAGN-1 and other LRDs.

5.2. Black hole–galaxy Scaling Relations

Other LRD observations have raised an additional challenge in terms of black hole to galaxy scaling relations. Because the sources are selected to be compact, even at high density there is a limit to their stellar mass. Providing our dust corrections are correct, we infer high ratios of black hole to galaxy mass. However, because of the high spectral resolution observations of RUBIES-BLAGN-1, we have an estimate of σ_* based on the narrow line widths. Much like the broad-line sources highlighted in Maiolino et al. (2023), we see some evidence that the black hole mass is in accord with local $M_{\text{BH}} - \sigma_*$ scaling relations, even if the stellar mass has not yet caught up. With only a handful of objects it is hard to draw any concrete conclusions yet, but perhaps these relations support the suggestion of Silk et al. (2024) that the high densities in these early galaxies trigger black hole growth and star formation.

5.3. An Ionized Outflow Traced by He I Absorption

We have reported a detection of an absorption feature in the wings of He I $\lambda 1.083 \mu\text{m}$ in the G395M spectrum. Being in the rest-frame near-IR, studies on this line are scarce, even in nearby objects (Hutchings et al. 2002; Leighly et al. 2011; Zhang et al. 2017; Landt et al. 2019; Wildy et al. 2021). At higher redshifts, outflows in AGN have mainly been probed in the highly ionized phase (e.g., C IV absorption or [O III] emission), while results on neutral gas emission ([C II]) have yielded ambiguous results (e.g., Bischetti et al. 2019; Novak et al. 2020). Our observation thus offers a new look at the outflow properties of LRDs.

The ionized gas outflow in RUBIES-BLAGN-1 has a similar velocity to emission line outflows detected in AGN host galaxies at $z \sim 2$ (e.g., Förster Schreiber et al. 2019), but the physical scale of the outflow appears to be much smaller ($\lesssim 100 \text{ pc}$). However, the size of the outflow is poorly constrained in our analysis because the He I absorption strength is virtually independent of the gas density (e.g., Ji et al. 2015).

The most powerful outflow in our model grid has a kinetic luminosity $< 1\%$ of the bolometric luminosity ($\sim 10^{47}$ erg s $^{-1}$). This suggests that this outflow alone is unlikely to be a significant source of feedback, including regulating accretion onto the black hole or star formation in the host galaxy, but there may be additional outflow mass hidden in other phases (Belli et al. 2023).

In the future, observations covering the H α or H β line at higher spectral resolution would help to better constrain the gas density in the absorbing material (e.g., Wildy et al. 2016). Measurements of absorption column densities in lower ionization absorption lines such as Na I D would also provide stronger constraints on the ionization structure within the absorbing medium. In addition, higher resolution observations covering [O III] λ 5007 (Liu et al. 2013) would allow us to search for larger scale ionized outflows manifesting as broad forbidden emission line components and examine the relationship between these kpc-scale outflows and the smaller He I outflow seen in our observations.

5.4. Final Remarks

The red objects discovered by JWST continue to challenge the standard views surrounding the evolution of black holes and galaxies. This paper presents an in-depth analysis of an LRD that has both broad lines and JWST/MIRI detections, an occurrence that was observed only once previously. The lower redshift of RUBIES-BLAGN-1 provides a better coverage at the rest-frame mid-IR, making the lack of torus emission more evident. While it remains uncertain whether RUBIES-BLAGN-1 represents the typical properties of LRDs in terms of the inferred characteristics of the host galaxy, AGN, and outflows, this work demonstrates a promising prospect for understanding the nature of the red sources. The RUBIES program will obtain a statistical sample in the near future, and we plan to extend our modeling framework to perform a systematic investigation, which will contribute to an important chapter of the narrative of black hole growth.

ACKNOWLEDGMENTS

B.W. and J.L. acknowledge support from JWST-GO-04233.009-A. R.L.D. is supported by the Australian Research Council through the Discovery Early Career Researcher Award (DECRA) Fellowship DE240100136 funded by the Australian Government. T.B.M. was supported by a CIERA postdoctoral fellowship. The Cosmic Dawn Center is funded by the Danish National Research Foundation (DNRF) under grant #140. This research was supported by the International Space Science Institute (ISSI) in Bern, through ISSI International

Team project #562 (First Light at Cosmic Dawn: Exploiting the James Webb Space Telescope Revolution). Computations for this research were performed on the Pennsylvania State University’s Institute for Computational and Data Sciences’ Roar supercomputer. This publication made use of the NASA Astrophysical Data System for bibliographic information.

Facilities: HST (ACS, WFC3), JWST (NIRCam, NIRSpec), Spitzer (MIPS), Herschel (PACS, SPIRE)

Software: Astropy (Astropy Collaboration et al. 2022), Cloudy (Ferland et al. 2017), emcee (Foreman-Mackey et al. 2013), dynesty (Speagle 2020), Matplotlib (Hunter 2007), msaexp (Brammer 2023b), NumPy (Harris et al. 2020), NUTS (Hoffman et al. 2014; Phan et al. 2019), photutils (Bradley et al. 2023), Prospector (Johnson et al. 2021), pysersic (Pasha & Miller 2023), SciPy (Virtanen et al. 2020)

APPENDIX

A. MORPHOLOGY

We perform a morphological analysis of RUBIES-BLAGN-1 in the short wavelength filter F115W and the long wavelength filter F277W, which probe the rest-frame UV (~ 0.28 μ m) and rest-frame optical (~ 0.68 μ m), respectively. We create a custom mosaic for the F115W imaging, largely following the procedure described in Section 2, but drizzled to an improved pixel scale of 0.02". Empirical PSFs are constructed from non-saturated stars on the 0.02" mosaic for F115W, and the 0.04" mosaic for F277W (A. Weibel et al. in prep).

We first measure the radial surface brightness profiles using the `photutils.profiles` module (Bradley et al. 2023) with circular apertures that are one pixel wide, ranging from 0 – 15 pixels. As seen from Figure 8, the surface brightness profile of RUBIES-BLAGN-1 extends beyond the profile of the PSF in the rest-frame UV (F115W), indicating that it is indeed spatially extended. Conversely, in F277W the brightness profile of RUBIES-BLAGN-1 and the PSF show no significant differences, indicating that it is a point source at longer wavelengths.

Second, we utilize `pysersic` (Pasha & Miller 2023) to fit a Sérsic profile (Sersic 1968) to the images. We assume a uniform prior for the effective radius (between 0.25 to 10 pixels) and a uniform prior on Sérsic index (between 0.65 to 4). We use the No-U-Turn Sampler (NUTS; Hoffman et al. 2014; Phan et al. 2019) to explore the posterior distribution of the morphological parameters with four chains and one thousand warm-up steps, and then five thousand sampling steps for each filter.

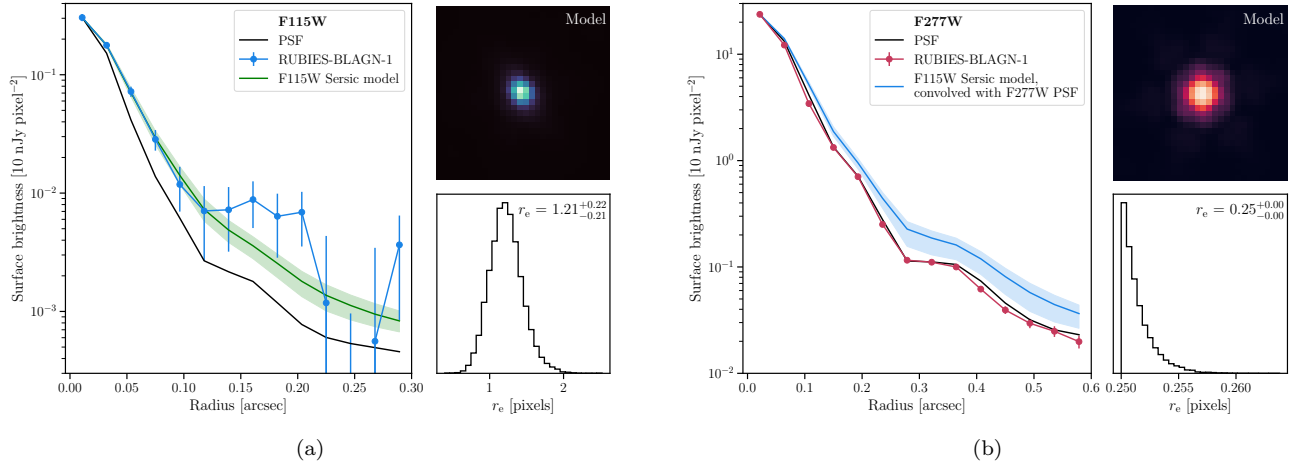


Figure 8. Morphological modeling. (a) The observed and modeled radial surface brightness profiles of RUBIES-BLAGN-1 in F115W are shown in blue and green, respectively. The PSF profile, scaled to the source, is over-plotted in black. The upper right panel shows the Sérsic model fit, and the lower right panel shows the marginalized posterior distribution of the effective radius in pixels. (b) Same as the left panel, but for F277W. In blue, we also show the surface brightness profile measured by sampling from the posteriors of the Sérsic fit in F115W and convolving with the F277W PSF. The median is plotted as a blue curve, with shaded regions indicating the 1σ uncertainty, and demonstrates that RUBIES-BLAGN-1 is slightly extended in the rest-frame UV, but unresolved at longer wavelengths where emission from the AGN dominates.

Consistent with our findings based on the surface brightness profiles, we find RUBIES-BLAGN-1 to be marginally resolved with an effective radius $r_e = 1.21 \pm 0.21$ pixel ($0.024 \pm 0.004''$) in the F115W filter. The Sérsic index is largely unconstrained but the posterior displays a slight preference for $n > 2$. Focusing on the 30×30 pixel region centered on RUBIES-BLAGN-1, the maximum a-posteriori Sérsic model shows a lower χ^2 by 15% compared to the value when modeling it solely as a point source. In F277W, RUBIES-BLAGN-1 is unresolved with an inferred $r_e \leq 0.3$ pixel ($0.012''$). The Sérsic model shows no improvement in the χ^2 values compared to modelling it as a point source. Both Sérsic models and marginalized posteriors for the effective radii are included in Figure 8.

Furthermore, we draw 500 posterior samples from the F115W Sérsic fit, convolve the model images with the F277W PSF, and measure the surface brightness profiles. The median and the 1σ widths are over-plotted in blue in Figure 8(b). The resulting model profile is slightly extended compared to the PSF: therefore, if the rest-frame optical light of RUBIES-BLAGN-1 were as extended as the rest-frame UV, then it should also be marginally resolved in F277W. Crucially, we do not observe such a difference, which implies that the UV and rest-frame optical indeed trace different physical components.

To summarize, we find that RUBIES-BLAGN-1 is marginally resolved in F115W, but unresolved in F277W. This analysis is independent of our SED mod-

eling, but, interestingly, consistent with our SED modeling results (§ 4.3): the emission in the rest-frame UV originates from the host galaxy and thus is extended spatially, whereas the rest-frame optical emission is dominated by the AGN that is point-like in nature.

B. ALTERNATIVE SED MODELS

Four alternative SED models are considered to offer insight into the systematic uncertainties. The inferred key parameters from each model are summarized in Table 4. The galaxy-only model, which is used to argue in favor of our fiducial composite model in Section 4.2, is not discussed again here.

B.1. AGN Only

We construct a simple AGN model, composed solely of accretion disk and torus emissions. The best-fit is shown in Figures 9(a). This AGN-only model fails to describe the blue UV slope, as expected given the intrinsic spectral shape of the AGN accretion disk. Combining this result with the galaxy-only model supports the inference from our fiducial model that the observed spectrum of RUBIES-BLAGN-1 comprises light from the AGN and its host galaxy. We note, however, that a pure-AGN model with a scattered light component (Greene et al. 2023) remains a possibility.

B.2. Dust

Table 4. Inferred Key Parameters Assuming Alternative SED Models

Parameter	Galaxy-only	AGN-only	Two-component Dust	UV Continuum Masked
$\log M_*/M_\odot$	$11.05^{+0.08}_{-0.08}$	—	$9.53^{+0.22}_{-0.18}$	$9.50^{+0.20}_{-0.24}$
Age [Gyr]	$0.80^{+0.11}_{-0.19}$	—	$0.74^{+0.10}_{-0.11}$	$0.68^{+0.19}_{-0.19}$
SFR [$M_\odot \text{ yr}^{-1}$]	$164.20^{+41.77}_{-24.39}$	—	$1.47^{+1.60}_{-0.60}$	$2.76^{+1.98}_{-1.17}$
$\log \text{sSFR}/\text{yr}^{-1}$	$-8.84^{+0.13}_{-0.10}$	—	$-9.32^{+0.18}_{-0.23}$	$-9.00^{+0.24}_{-0.33}$
$\log Z/Z_\odot$	$-1.27^{+0.17}_{-0.14}$	—	$-1.65^{+0.36}_{-0.24}$	$-0.93^{+0.55}_{-0.48}$
$\hat{\tau}_{\text{dust},1}$	$1.23^{+0.37}_{-0.33}$	—	$2.50^{+0.96}_{-1.36}$	—
f_{obrun}	$0.47^{+0.31}_{-0.18}$	—	$0.32^{+0.33}_{-0.22}$	—
$\hat{\tau}_{\text{dust},2}$	$2.64^{+0.18}_{-0.16}$	$3.14^{+0.17}_{-0.24}$	$2.62^{+0.06}_{-0.06}$	$0.90^{+0.48}_{-0.31}$
$n_{\text{dust},2}$	$-0.34^{+0.16}_{-0.14}$	$0.02^{+0.03}_{-0.02}$	$-0.97^{+0.03}_{-0.02}$	$-0.86^{+0.20}_{-0.10}$
f_{nodust}	$0.01^{+0.00}_{-0.00}$	$0.50^{+0.19}_{-0.26}$	$0.59^{+0.24}_{-0.26}$	$0.37^{+0.34}_{-0.25}$
$\log f_{\text{AGN},7500\text{\AA}}$	—	—	$1.13^{+0.10}_{-0.16}$	$0.97^{+0.16}_{-0.15}$
$\log f_{\text{AGN},\text{torus}}$	—	—	$-2.50^{+0.63}_{-0.13}$	$-2.31^{+0.22}_{-0.02}$
$\hat{\tau}_{\text{torus}}$	—	—	$7.66^{+36.20}_{-2.06}$	$9.86^{+9.14}_{-3.57}$
$\hat{\tau}_{\text{dust},4}$	—	$0.52^{+0.29}_{-0.18}$	—	$2.20^{+0.39}_{-0.47}$
$n_{\text{dust},4}$	—	$-1.07^{+0.12}_{-0.13}$	—	$-1.43^{+0.26}_{-0.20}$

The redness of RUBIES-BLAGN-1 does not necessarily mean that the AGN receives additional attenuation. We thus consider the standard dust model, where dust reddening of the stellar light is described by two components (Charlot & Fall 2000) with a flexible dust attenuation curve (Noll et al. 2009). As in the fiducial model, a fraction of the stellar light is allowed to be seen outside the diffuse dust. In addition, a fraction of the young stellar light is allowed to be not attenuated by the birth cloud, which represents runaway OB stars or escaping ionizing radiation.

This model infers significant dust presence, driven by the red continuum as in the fiducial model. However, without the additional attenuation experienced only by the AGN, $\sim 40\%$ of the young stars and $\sim 60\%$ of all stars are required to be located outside the birth cloud and the diffuse dust, respectively, to produce the UV excess. It is less intuitive to reconcile this situation where

a significant fraction of the stars remains unaffected by dust attenuation while the AGN experiences substantial attenuation.

B.3. Fitting the Rest Optical Spectrum Only

It is possible that the UV continuum is of non-stellar origin. We test this hypothesis by masking the UV, and fit the red continuum with the fiducial model. This setting fails to predict an UV excess, meaning that the UV continuum does not have to be composed of starlight. It can, for example, be the scattered light from the AGN (Greene et al. 2023). Crucially, the inferred stellar mass in this case is about the same as that from the fiducial model, suggesting that the UV continuum has less constraining power. While we can add in a non-stellar component for the UV, this result means that the extra UV component will not add much information under the assumed dust model, except improving the χ^2 .

REFERENCES

- Abramowicz, M. A., Czerny, B., Lasota, J. P., & Szuszkiewicz, E. 1988, ApJ, 332, 646, doi: [10.1086/166683](https://doi.org/10.1086/166683)
- Asmus, D., Hönig, S. F., & Gandhi, P. 2016, ApJ, 822, 109, doi: [10.3847/0004-637X/822/2/109](https://doi.org/10.3847/0004-637X/822/2/109)
- Astropy Collaboration, Price-Whelan, A. M., Lim, P. L., et al. 2022, ApJ, 935, 167, doi: [10.3847/1538-4357/ac7c74](https://doi.org/10.3847/1538-4357/ac7c74)
- Baggen, J. F. W., van Dokkum, P., Labbé, I., et al. 2023, ApJL, 955, L12, doi: [10.3847/2041-8213/acf5ef](https://doi.org/10.3847/2041-8213/acf5ef)
- Barro, G., Perez-Gonzalez, P. G., Kocevski, D. D., et al. 2023, arXiv e-prints, arXiv:2305.14418, doi: [10.48550/arXiv.2305.14418](https://doi.org/10.48550/arXiv.2305.14418)
- Barrufet, L., Oesch, P. A., Weibel, A., et al. 2023, MNRAS, 522, 449, doi: [10.1093/mnras/stad947](https://doi.org/10.1093/mnras/stad947)
- Belli, S., Park, M., Davies, R. L., et al. 2023, arXiv e-prints, arXiv:2308.05795, doi: [10.48550/arXiv.2308.05795](https://doi.org/10.48550/arXiv.2308.05795)
- Bertin, E., & Arnouts, S. 1996, A&AS, 117, 393, doi: [10.1051/aas:1996164](https://doi.org/10.1051/aas:1996164)

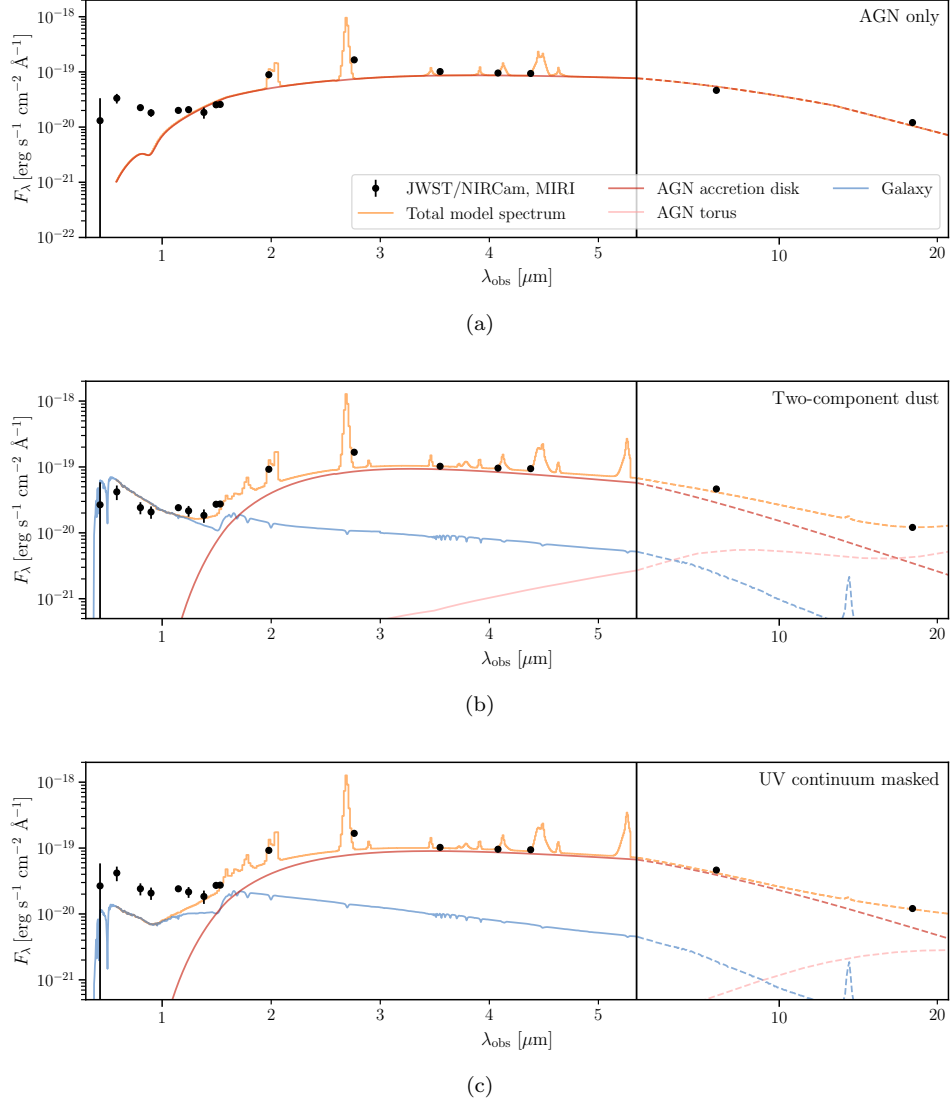


Figure 9. Alternative SED models. (a) Fitting with AGN light only. (b) Fitting with the standard two-component dust model. (c) Fitting only the rest optical spectrum using the fiducial model. In each panel, the best-fit total model spectrum, with the marginalized emission lines added, is plotted in orange. The model spectra of the AGN accretion disk, torus, and the galaxy are plotted in red, pink, and blue, respectively. The photometric observations are included as black dots, but the observed spectrum is omitted for clarity.

Bischetti, M., Maiolino, R., Carniani, S., et al. 2019, *A&A*, 630, A59, doi: [10.1051/0004-6361/201833557](https://doi.org/10.1051/0004-6361/201833557)

Blandford, R. D., & McKee, C. F. 1982, *ApJ*, 255, 419, doi: [10.1086/159843](https://doi.org/10.1086/159843)

Bosman, S. E. I., Álvarez-Márquez, J., Colina, L., et al. 2023, arXiv e-prints, arXiv:2307.14414, doi: [10.48550/arXiv.2307.14414](https://doi.org/10.48550/arXiv.2307.14414)

Bradley, L., Sipőcz, B., Robitaille, T., et al. 2023, *astropy/photutils*: 1.8.0, 1.8.0, Zenodo, doi: [10.5281/zenodo.7946442](https://doi.org/10.5281/zenodo.7946442)

Brammer, G. 2023a, *grizli*, 1.9.11, Zenodo, doi: [10.5281/zenodo.1146904](https://doi.org/10.5281/zenodo.1146904)

—. 2023b, *msaexp: NIRSpec analysis tools*, 0.6.17, Zenodo, doi: [10.5281/zenodo.7299500](https://doi.org/10.5281/zenodo.7299500)

Brown, M. J. I., Duncan, K. J., Landt, H., et al. 2019, *MNRAS*, 489, 3351, doi: [10.1093/mnras/stz2324](https://doi.org/10.1093/mnras/stz2324)

Calzetti, D., Armus, L., Bohlin, R. C., et al. 2000, *ApJ*, 533, 682, doi: [10.1086/308692](https://doi.org/10.1086/308692)

Cappellari, M., Bacon, R., Bureau, M., et al. 2006, *MNRAS*, 366, 1126, doi: [10.1111/j.1365-2966.2005.09981.x](https://doi.org/10.1111/j.1365-2966.2005.09981.x)

Carnall, A. C., McLure, R. J., Dunlop, J. S., et al. 2023, *Nature*, 619, 716, doi: [10.1038/s41586-023-06158-6](https://doi.org/10.1038/s41586-023-06158-6)

Chabrier, G. 2003, *PASP*, 115, 763, doi: [10.1086/376392](https://doi.org/10.1086/376392)

- Charlot, S., & Fall, S. M. 2000, *ApJ*, 539, 718, doi: [10.1086/309250](https://doi.org/10.1086/309250)
- Chatzikos, M., Bianchi, S., Camilloni, F., et al. 2023, *RMxAA*, 59, 327, doi: [10.22201/ia.01851101p.2023.59.02.12](https://doi.org/10.22201/ia.01851101p.2023.59.02.12)
- Chisholm, J. R., Dodelson, S., & Kolb, E. W. 2003, *ApJ*, 596, 437, doi: [10.1086/377628](https://doi.org/10.1086/377628)
- Choi, J., Dotter, A., Conroy, C., et al. 2016, *ApJ*, 823, 102, doi: [10.3847/0004-637X/823/2/102](https://doi.org/10.3847/0004-637X/823/2/102)
- Conroy, C., & Gunn, J. E. 2010, *ApJ*, 712, 833, doi: [10.1088/0004-637X/712/2/833](https://doi.org/10.1088/0004-637X/712/2/833)
- Conroy, C., Gunn, J. E., & White, M. 2009, *ApJ*, 699, 486, doi: [10.1088/0004-637X/699/1/486](https://doi.org/10.1088/0004-637X/699/1/486)
- Culliton, C., Charlton, J., Eracleous, M., Ganguly, R., & Misawa, T. 2019, *MNRAS*, 488, 4690, doi: [10.1093/mnras/stz1642](https://doi.org/10.1093/mnras/stz1642)
- Davies, R., Baron, D., Shimizu, T., et al. 2020, *MNRAS*, 498, 4150, doi: [10.1093/mnras/staa2413](https://doi.org/10.1093/mnras/staa2413)
- de Graaff, A., Rix, H.-W., Carniani, S., et al. 2023, *arXiv e-prints*, arXiv:2308.09742, doi: [10.48550/arXiv.2308.09742](https://doi.org/10.48550/arXiv.2308.09742)
- Dotter, A. 2016, *ApJS*, 222, 8, doi: [10.3847/0067-0049/222/1/8](https://doi.org/10.3847/0067-0049/222/1/8)
- Draine, B. T., & Li, A. 2007, *ApJ*, 657, 810, doi: [10.1086/511055](https://doi.org/10.1086/511055)
- Dullemond, C. P., & van Bemmell, I. M. 2005, *A&A*, 436, 47, doi: [10.1051/0004-6361:20041763](https://doi.org/10.1051/0004-6361:20041763)
- Eenens, P. R. J., & Williams, P. M. 1994, *MNRAS*, 269, 1082, doi: [10.1093/mnras/269.4.1082](https://doi.org/10.1093/mnras/269.4.1082)
- Eisenstein, D. J., Willott, C., Alberts, S., et al. 2023, *arXiv e-prints*, arXiv:2306.02465, doi: [10.48550/arXiv.2306.02465](https://doi.org/10.48550/arXiv.2306.02465)
- Ferland, G. J., Chatzikos, M., Guzmán, F., et al. 2017, *RMxAA*, 53, 385, doi: [10.48550/arXiv.1705.10877](https://doi.org/10.48550/arXiv.1705.10877)
- Foreman-Mackey, D., Hogg, D. W., Lang, D., & Goodman, J. 2013, *PASP*, 125, 306, doi: [10.1086/670067](https://doi.org/10.1086/670067)
- Förster Schreiber, N. M., Übler, H., Davies, R. L., et al. 2019, *ApJ*, 875, 21, doi: [10.3847/1538-4357/ab0ca2](https://doi.org/10.3847/1538-4357/ab0ca2)
- Furtak, L. J., Zitrin, A., Plat, A., et al. 2023a, *ApJ*, 952, 142, doi: [10.3847/1538-4357/acdc9d](https://doi.org/10.3847/1538-4357/acdc9d)
- Furtak, L. J., Labbé, I., Zitrin, A., et al. 2023b, *arXiv e-prints*, arXiv:2308.05735, doi: [10.48550/arXiv.2308.05735](https://doi.org/10.48550/arXiv.2308.05735)
- Goulding, A. D., Greene, J. E., Setton, D. J., et al. 2023, *ApJL*, 955, L24, doi: [10.3847/2041-8213/acf7c5](https://doi.org/10.3847/2041-8213/acf7c5)
- Greene, J. E., & Ho, L. C. 2005, *ApJ*, 630, 122, doi: [10.1086/431897](https://doi.org/10.1086/431897)
- Greene, J. E., Labbe, I., Goulding, A. D., et al. 2023, *arXiv e-prints*, arXiv:2309.05714, doi: [10.48550/arXiv.2309.05714](https://doi.org/10.48550/arXiv.2309.05714)
- Grogin, N. A., Kocevski, D. D., Faber, S. M., et al. 2011, *ApJS*, 197, 35, doi: [10.1088/0067-0049/197/2/35](https://doi.org/10.1088/0067-0049/197/2/35)
- Grudić, M. Y., Hopkins, P. F., Quataert, E., & Murray, N. 2019, *MNRAS*, 483, 5548, doi: [10.1093/mnras/sty3386](https://doi.org/10.1093/mnras/sty3386)
- Hainline, L. J., Blain, A. W., Smail, I., et al. 2011, *ApJ*, 740, 96, doi: [10.1088/0004-637X/740/2/96](https://doi.org/10.1088/0004-637X/740/2/96)
- Hao, C.-N., Kennicutt, R. C., Johnson, B. D., et al. 2011, *ApJ*, 741, 124, doi: [10.1088/0004-637X/741/2/124](https://doi.org/10.1088/0004-637X/741/2/124)
- Hao, H., Elvis, M., Civano, F., et al. 2010, *ApJL*, 724, L59, doi: [10.1088/2041-8205/724/1/L59](https://doi.org/10.1088/2041-8205/724/1/L59)
- Harikane, Y., Zhang, Y., Nakajima, K., et al. 2023, *ApJ*, 959, 39, doi: [10.3847/1538-4357/ad029e](https://doi.org/10.3847/1538-4357/ad029e)
- Harris, C. R., Millman, K. J., van der Walt, S. J., et al. 2020, *Nature*, 585, 357, doi: [10.1038/s41586-020-2649-2](https://doi.org/10.1038/s41586-020-2649-2)
- Hinshaw, G., Larson, D., Komatsu, E., et al. 2013, *ApJS*, 208, 19, doi: [10.1088/0067-0049/208/2/19](https://doi.org/10.1088/0067-0049/208/2/19)
- Hoffman, M. D., Gelman, A., et al. 2014, *J. Mach. Learn. Res.*, 15, 1593
- Hönig, S. F., Beckert, T., Ohnaka, K., & Weigelt, G. 2006, *A&A*, 452, 459, doi: [10.1051/0004-6361:20054622](https://doi.org/10.1051/0004-6361:20054622)
- Hopkins, P. F., Murray, N., Quataert, E., & Thompson, T. A. 2010, *MNRAS*, 401, L19, doi: [10.1111/j.1745-3933.2009.00777.x](https://doi.org/10.1111/j.1745-3933.2009.00777.x)
- Hunter, J. D. 2007, *Computing in Science and Engineering*, 9, 90, doi: [10.1109/MCSE.2007.55](https://doi.org/10.1109/MCSE.2007.55)
- Hutchings, J. B., Crenshaw, D. M., Kraemer, S. B., et al. 2002, *AJ*, 124, 2543, doi: [10.1086/344080](https://doi.org/10.1086/344080)
- Ji, T., Zhou, H., Jiang, P., et al. 2015, *ApJ*, 800, 56, doi: [10.1088/0004-637X/800/1/56](https://doi.org/10.1088/0004-637X/800/1/56)
- Ji, Z., Williams, C. C., Suess, K. A., et al. 2024, *arXiv e-prints*, arXiv:2401.00934, doi: [10.48550/arXiv.2401.00934](https://doi.org/10.48550/arXiv.2401.00934)
- Jiang, L., Fan, X., Brandt, W. N., et al. 2010, *Nature*, 464, 380, doi: [10.1038/nature08877](https://doi.org/10.1038/nature08877)
- Johnson, B. D., Leja, J., Conroy, C., & Speagle, J. S. 2021, *ApJS*, 254, 22, doi: [10.3847/1538-4365/abef67](https://doi.org/10.3847/1538-4365/abef67)
- Kaspi, S., Smith, P. S., Netzer, H., et al. 2000, *ApJ*, 533, 631, doi: [10.1086/308704](https://doi.org/10.1086/308704)
- Killi, M., Watson, D., Brammer, G., et al. 2023, *arXiv e-prints*, arXiv:2312.03065, doi: [10.48550/arXiv.2312.03065](https://doi.org/10.48550/arXiv.2312.03065)
- Kim, D., Im, M., Glikman, E., Woo, J.-H., & Urrutia, T. 2015, *ApJ*, 812, 66, doi: [10.1088/0004-637X/812/1/66](https://doi.org/10.1088/0004-637X/812/1/66)
- Kim, D., Im, M., & Kim, M. 2010, *ApJ*, 724, 386, doi: [10.1088/0004-637X/724/1/386](https://doi.org/10.1088/0004-637X/724/1/386)
- Kocevski, D. D., Hasinger, G., Brightman, M., et al. 2018, *ApJS*, 236, 48, doi: [10.3847/1538-4365/aab9b4](https://doi.org/10.3847/1538-4365/aab9b4)
- Kocevski, D. D., Onoue, M., Inayoshi, K., et al. 2023, *ApJL*, 954, L4, doi: [10.3847/2041-8213/ace5a0](https://doi.org/10.3847/2041-8213/ace5a0)

- Koekemoer, A. M., Faber, S. M., Ferguson, H. C., et al. 2011, *ApJS*, 197, 36, doi: [10.1088/0067-0049/197/2/36](https://doi.org/10.1088/0067-0049/197/2/36)
- Kokorev, V., Fujimoto, S., Labbe, I., et al. 2023, *ApJL*, 957, L7, doi: [10.3847/2041-8213/ad037a](https://doi.org/10.3847/2041-8213/ad037a)
- Kubota, A., & Done, C. 2019, *MNRAS*, 489, 524, doi: [10.1093/mnras/stz2140](https://doi.org/10.1093/mnras/stz2140)
- Labbé, I., Greene, J. E., Bezanson, R., et al. 2023a, *arXiv e-prints*, arXiv:2306.07320, doi: [10.48550/arXiv.2306.07320](https://doi.org/10.48550/arXiv.2306.07320)
- Labbé, I., van Dokkum, P., Nelson, E., et al. 2023b, *Nature*, 616, 266, doi: [10.1038/s41586-023-05786-2](https://doi.org/10.1038/s41586-023-05786-2)
- Lacy, M., Storrie-Lombardi, L. J., Sajina, A., et al. 2004, *ApJS*, 154, 166, doi: [10.1086/422816](https://doi.org/10.1086/422816)
- Laha, S., Reynolds, C. S., Reeves, J., et al. 2021, *Nature Astronomy*, 5, 13, doi: [10.1038/s41550-020-01255-2](https://doi.org/10.1038/s41550-020-01255-2)
- Landt, H., Ward, M. J., Peterson, B. M., et al. 2013, *MNRAS*, 432, 113, doi: [10.1093/mnras/stt421](https://doi.org/10.1093/mnras/stt421)
- Landt, H., Ward, M. J., Kynoch, D., et al. 2019, *MNRAS*, 489, 1572, doi: [10.1093/mnras/stz2212](https://doi.org/10.1093/mnras/stz2212)
- Laurent, O., Mirabel, I. F., Charmandaris, V., et al. 2000, *A&A*, 359, 887, doi: [10.48550/arXiv.astro-ph/0005376](https://doi.org/10.48550/arXiv.astro-ph/0005376)
- Leighly, K. M., Dietrich, M., & Barber, S. 2011, *ApJ*, 728, 94, doi: [10.1088/0004-637X/728/2/94](https://doi.org/10.1088/0004-637X/728/2/94)
- Leja, J., Johnson, B. D., Conroy, C., & van Dokkum, P. 2018, *ApJ*, 854, 62, doi: [10.3847/1538-4357/aaa8db](https://doi.org/10.3847/1538-4357/aaa8db)
- Leja, J., Johnson, B. D., Conroy, C., van Dokkum, P. G., & Byler, N. 2017, *ApJ*, 837, 170, doi: [10.3847/1538-4357/aa5ffe](https://doi.org/10.3847/1538-4357/aa5ffe)
- Libralato, M., Argyriou, I., Dicken, D., et al. 2023, *arXiv e-prints*, arXiv:2311.12145, doi: [10.48550/arXiv.2311.12145](https://doi.org/10.48550/arXiv.2311.12145)
- Liu, G., Zakamska, N. L., Greene, J. E., Nesvadba, N. P. H., & Liu, X. 2013, *MNRAS*, 436, 2576, doi: [10.1093/mnras/stt1755](https://doi.org/10.1093/mnras/stt1755)
- Lyu, J., & Rieke, G. 2022, *Universe*, 8, 304, doi: [10.3390/universe8060304](https://doi.org/10.3390/universe8060304)
- Lyu, J., Rieke, G. H., & Shi, Y. 2017, *ApJ*, 835, 257, doi: [10.3847/1538-4357/835/2/257](https://doi.org/10.3847/1538-4357/835/2/257)
- Maiolino, R., Scholtz, J., Curtis-Lake, E., et al. 2023, *arXiv e-prints*, arXiv:2308.01230, doi: [10.48550/arXiv.2308.01230](https://doi.org/10.48550/arXiv.2308.01230)
- Mathews, W. G., & Ferland, G. J. 1987, *ApJ*, 323, 456, doi: [10.1086/165843](https://doi.org/10.1086/165843)
- Matthee, J., Naidu, R. P., Brammer, G., et al. 2023, *arXiv e-prints*, arXiv:2306.05448, doi: [10.48550/arXiv.2306.05448](https://doi.org/10.48550/arXiv.2306.05448)
- Misawa, T., Charlton, J. C., Eracleous, M., et al. 2007, *ApJS*, 171, 1, doi: [10.1086/513713](https://doi.org/10.1086/513713)
- Mor, R., & Trakhtenbrot, B. 2011, *ApJL*, 737, L36, doi: [10.1088/2041-8205/737/2/L36](https://doi.org/10.1088/2041-8205/737/2/L36)
- Nenkova, M., Sirocky, M. M., Ivezić, Ž., & Elitzur, M. 2008a, *ApJ*, 685, 147, doi: [10.1086/590482](https://doi.org/10.1086/590482)
- Nenkova, M., Sirocky, M. M., Nikutta, R., Ivezić, Ž., & Elitzur, M. 2008b, *ApJ*, 685, 160, doi: [10.1086/590483](https://doi.org/10.1086/590483)
- Noboriguchi, A., Inoue, A. K., Nagao, T., Toba, Y., & Misawa, T. 2023, *ApJL*, 959, L14, doi: [10.3847/2041-8213/ad0e00](https://doi.org/10.3847/2041-8213/ad0e00)
- Noll, S., Burgarella, D., Giovannoli, E., et al. 2009, *A&A*, 507, 1793, doi: [10.1051/0004-6361/200912497](https://doi.org/10.1051/0004-6361/200912497)
- Novak, M., Venemans, B. P., Walter, F., et al. 2020, *ApJ*, 904, 131, doi: [10.3847/1538-4357/abc33f](https://doi.org/10.3847/1538-4357/abc33f)
- Pacucci, F., & Loeb, A. 2024, *arXiv e-prints*, arXiv:2401.04159, doi: [10.48550/arXiv.2401.04159](https://doi.org/10.48550/arXiv.2401.04159)
- Pan, X., Zhou, H., Liu, W., et al. 2019, *ApJ*, 883, 173, doi: [10.3847/1538-4357/ab40b5](https://doi.org/10.3847/1538-4357/ab40b5)
- Pasha, I., & Miller, T. B. 2023, *The Journal of Open Source Software*, 8, 5703, doi: [10.21105/joss.05703](https://doi.org/10.21105/joss.05703)
- Pérez-González, P. G., Barro, G., Rieke, G. H., et al. 2024, *arXiv e-prints*, arXiv:2401.08782, doi: [10.48550/arXiv.2401.08782](https://doi.org/10.48550/arXiv.2401.08782)
- Phan, D., Pradhan, N., & Jankowiak, M. 2019, in *Program Transformations for ML Workshop at NeurIPS 2019*. <https://openreview.net/forum?id=H1g1niFhIB>
- Richards, G. T., Lacy, M., Storrie-Lombardi, L. J., et al. 2006, *ApJS*, 166, 470, doi: [10.1086/506525](https://doi.org/10.1086/506525)
- Rupke, D. S., Veilleux, S., & Sanders, D. B. 2005, *ApJS*, 160, 115, doi: [10.1086/432889](https://doi.org/10.1086/432889)
- Rupke, D. S. N., Gültekin, K., & Veilleux, S. 2017, *ApJ*, 850, 40, doi: [10.3847/1538-4357/aa94d1](https://doi.org/10.3847/1538-4357/aa94d1)
- Sánchez-Blázquez, P., Peletier, R. F., Jiménez-Vicente, J., et al. 2006, *MNRAS*, 371, 703, doi: [10.1111/j.1365-2966.2006.10699.x](https://doi.org/10.1111/j.1365-2966.2006.10699.x)
- Sanders, D. B., Phinney, E. S., Neugebauer, G., Soifer, B. T., & Matthews, K. 1989, *ApJ*, 347, 29, doi: [10.1086/168094](https://doi.org/10.1086/168094)
- Savage, B. D., & Sembach, K. R. 1991, *ApJ*, 379, 245, doi: [10.1086/170498](https://doi.org/10.1086/170498)
- Sawicki, M. 2002, *AJ*, 124, 3050, doi: [10.1086/344682](https://doi.org/10.1086/344682)
- Sersic, J. L. 1968, *Cordoba*
- Setton, D. J., Khullar, G., Miller, T. B., et al. 2024, *arXiv e-prints*, arXiv:2402.05664, doi: [10.48550/arXiv.2402.05664](https://doi.org/10.48550/arXiv.2402.05664)
- Shen, X., Hopkins, P. F., Faucher-Giguère, C.-A., et al. 2020, *MNRAS*, 495, 3252, doi: [10.1093/mnras/staa1381](https://doi.org/10.1093/mnras/staa1381)
- Shen, Y., & Kelly, B. C. 2012, *ApJ*, 746, 169, doi: [10.1088/0004-637X/746/2/169](https://doi.org/10.1088/0004-637X/746/2/169)
- Silk, J., Begelman, M. C., Norman, C., Nusser, A., & Wyse, R. F. G. 2024, *ApJL*, 961, L39, doi: [10.3847/2041-8213/ad1bf0](https://doi.org/10.3847/2041-8213/ad1bf0)

- Son, S., Kim, M., & Ho, L. C. 2023, *ApJ*, 953, 175,
doi: [10.3847/1538-4357/ace165](https://doi.org/10.3847/1538-4357/ace165)
- Speagle, J. S. 2020, *MNRAS*, 493, 3132,
doi: [10.1093/mnras/staa278](https://doi.org/10.1093/mnras/staa278)
- Speagle, J. S., Steinhardt, C. L., Capak, P. L., & Silverman, J. D. 2014, *ApJS*, 214, 15,
doi: [10.1088/0067-0049/214/2/15](https://doi.org/10.1088/0067-0049/214/2/15)
- Stalevski, M., Tristram, K. R. W., & Asmus, D. 2019, *MNRAS*, 484, 3334, doi: [10.1093/mnras/stz220](https://doi.org/10.1093/mnras/stz220)
- Stern, J., & Laor, A. 2012, *MNRAS*, 423, 600,
doi: [10.1111/j.1365-2966.2012.20901.x](https://doi.org/10.1111/j.1365-2966.2012.20901.x)
- Stevens, I. R., & Howarth, I. D. 1999, *MNRAS*, 302, 549,
doi: [10.1046/j.1365-8711.1999.02151.x](https://doi.org/10.1046/j.1365-8711.1999.02151.x)
- Temple, M. J., Hewett, P. C., & Banerji, M. 2021, *MNRAS*, 508, 737, doi: [10.1093/mnras/stab2586](https://doi.org/10.1093/mnras/stab2586)
- Urrutia, T., Lacy, M., Spoon, H., et al. 2012, *ApJ*, 757, 125, doi: [10.1088/0004-637X/757/2/125](https://doi.org/10.1088/0004-637X/757/2/125)
- Valentino, F., Brammer, G., Gould, K. M. L., et al. 2023, *ApJ*, 947, 20, doi: [10.3847/1538-4357/acbefa](https://doi.org/10.3847/1538-4357/acbefa)
- Vanden Berk, D. E., Richards, G. T., Bauer, A., et al. 2001, *AJ*, 122, 549, doi: [10.1086/321167](https://doi.org/10.1086/321167)
- Vidal-García, A., Plat, A., Curtis-Lake, E., et al. 2024, *MNRAS*, 527, 7217, doi: [10.1093/mnras/stad3252](https://doi.org/10.1093/mnras/stad3252)
- Virtanen, P., Gommers, R., Oliphant, T. E., et al. 2020, *Nature Methods*, 17, 261, doi: [10.1038/s41592-019-0686-2](https://doi.org/10.1038/s41592-019-0686-2)
- Wang, B., Fujimoto, S., Labbé, I., et al. 2023a, *ApJL*, 957, L34, doi: [10.3847/2041-8213/acf07](https://doi.org/10.3847/2041-8213/acf07)
- Wang, B., Leja, J., Bezanson, R., et al. 2023b, *ApJL*, 944, L58, doi: [10.3847/2041-8213/acba99](https://doi.org/10.3847/2041-8213/acba99)
- Wang, B., Leja, J., Labbé, I., et al. 2024, *ApJS*, 270, 12, doi: [10.3847/1538-4365/ad0846](https://doi.org/10.3847/1538-4365/ad0846)
- Wang, F., Fan, X., Yang, J., et al. 2021, *ApJ*, 908, 53, doi: [10.3847/1538-4357/abcc5e](https://doi.org/10.3847/1538-4357/abcc5e)
- Whitaker, K. E., Franx, M., Leja, J., et al. 2014, *ApJ*, 795, 104, doi: [10.1088/0004-637X/795/2/104](https://doi.org/10.1088/0004-637X/795/2/104)
- Wildy, C., Landt, H., Goad, M. R., Ward, M., & Collinson, J. S. 2016, *MNRAS*, 461, 2085, doi: [10.1093/mnras/stw1403](https://doi.org/10.1093/mnras/stw1403)
- Wildy, C., Landt, H., Ward, M. J., Czerny, B., & Kynoch, D. 2021, *MNRAS*, 500, 2063, doi: [10.1093/mnras/staa3301](https://doi.org/10.1093/mnras/staa3301)
- Williams, C. C., Alberts, S., Ji, Z., et al. 2023, *arXiv e-prints*, arXiv:2311.07483, doi: [10.48550/arXiv.2311.07483](https://doi.org/10.48550/arXiv.2311.07483)
- Wright, L., Whitaker, K. E., Weaver, J. R., et al. 2023, *arXiv e-prints*, arXiv:2311.05394, doi: [10.48550/arXiv.2311.05394](https://doi.org/10.48550/arXiv.2311.05394)
- Yang, G., Boquien, M., Buat, V., et al. 2020, *MNRAS*, 491, 740, doi: [10.1093/mnras/stz3001](https://doi.org/10.1093/mnras/stz3001)
- Zakamska, N. L., & Greene, J. E. 2014, *MNRAS*, 442, 784, doi: [10.1093/mnras/stu842](https://doi.org/10.1093/mnras/stu842)
- Zhang, S., Zhou, H., Shi, X., et al. 2017, *ApJ*, 845, 126, doi: [10.3847/1538-4357/aa8223](https://doi.org/10.3847/1538-4357/aa8223)